A CPFEM based study to understand the void growth in high strength dual-phase Titanium alloy (Ti-10V-2Fe-3Al)

Umair Asim[1], M Amir Siddiq[1], Mehmet E Kartal[1]

[1] School of Engineering, University of Aberdeen, Fraser Noble Building, AB24 3UE, Aberdeen, United Kingdom

E-mail: amir.siddiq@abdn.ac.uk

Abstract

High strength titanium alloys are generally used in widespread applications ranging over, but not limited to biomedical, aerospace, automotive, marine, oil and gas, and energy. Besides other manufacturing processes, forming is one of the common manufacturing process used to produce components out of these alloys. Forming processes generally involve significant plastic deformation of material under complex multiaxial loading conditions. Titanium alloys undergo considerable plastic deformation before failure while later is governed by the mechanisms of void nucleation, growth and coalescence. A number of titanium alloys used for high strength applications are multiphase alloys having α and β phases. It has been reported in the past that the voids tend to nucleate on the phase boundaries. This study is focused on understanding the growth of the nucleated voids at two selected locations in a dual phase titanium alloy (Ti-10V-2Fe-3Al); globular α phase (hexagonal closed pack, HCP) and at the interface of lamellar α and β phases (α - HCP and β – body centred cubic, BCC). This is one of the very few 3D representative volume element (RVE) study of void growth in single crystal titanium (HCP), carried out using crystal plasticity finite element modelling (CPFEM) at higher triaxialities (ranging 1/3-3) and the first one on the interface of bicrystals with different crystal symmetry. The effects of initial porosity and crystal orientation on void growth in single crystal (α - HCP) has been studied and it is found that both affects void growth considerably. An effort has been made to explain the physics behind it. In the second part, growth in a void at the interface of two distinct single crystals (α - HCP and β –BCC) was studied. The effects of Burgers orientation relationship (BOR) variant of the two phases, initial porosity, and phase boundary inclination (PBI) on void growth is investigated. It is found that the PBI has a very strong impact on the void growth. The effect of initial porosity is similar to the void growth in single crystals. Choice of BOR variant affected the void growth in moderate triaxialities.

Keywords: Void growth, crystal plasticity, multiphase titanium alloys, ductile damage

1. Introduction

Titanium alloys are one of the best candidate for industrial applications where corrosion resistant and high strength material is sought which can perform in severe operating conditions, some examples include; high strength aerospace structures, performance automotive parts, marine applications, and oil & gas applications. Demand of α-β titanium alloys supersedes all the other type of titanium alloys because of their unique set of mechanical properties, such as higher yield strength, ductility, formability, high and low cycle fatigue performance and fracture toughness. These alloys undergo ductile failure which is governed by void nucleation, growth and coalescence (Lütjering and Williams, 2007; Peters et al., 2003; Xie et al., 2018).

Difference in ductility of various solution treated and aged conditions of Ti-10V-2Fe-3Al alloy was presented by the Terlinde et al. (1980). Terlinde et al. (1983) found the relation between the

quantitative combinations of various α-variants present and the possible void nucleation site. A crack growth model along the grain boundary α was presented based on various parameters like grain size, yield strength, plastic zone size, and crack deviation by Terlinde et al. (1988). The effect of microstructural defects and inclusion in powder-processed Ti-10V-2Fe-3Al alloy in fracture toughness was studied by Moody et al. (1989), it was found that the small inclusions do not participate in fracture process whereas the inclusions which partook in fracturing grew in size and became the void nucleation sites as per ductile fracture theory. Zeng & Zhou (1999) studied the effect of β flecks as the possible crack nucleation site in Ti-10V-2Fe-3Al. β flecks were found to be the nucleation site of crack which will further go on to grow and coalesce to ultimately fail the material in tensile loading while in case of low-cycle fatigue they act as crack nucleation sites. Bhattacharjee et al. (2006) investigated the effect of grain sizes on fracture toughness of the alloys in Ti-10V-2Fe-3Al alloy and reported that failure was by the mechanism of void nucleation, growth and coalescence. Work by Kanamori et al. (2002; 2002; 2007; 2013) comprehensively examined the failure in titanium alloys containing different morphologies of α in β matrix and reported that the voids almost always nucleate at the interface of α/β boundaries.

It has been established theoretically and analytically that ductile materials fail under the influence of void nucleation, void growth, and void coalescence (Gurson, 1977; Rice and Tracey, 1969; Tvergaard and Needleman, 1984). Void nucleation sites can vary depending on the type of material. They can nucleate at the grain boundaries (Hull and Rimmer, 1959), sub-grain boundaries (Terlinde et al., 1983), around precipitates and inclusions (Hutchinson and Tvergaard, 1989), and places where the density of accumulated slips is very high (Fleck and Hutchinson, 1993). Nucleated voids can then grow depending upon the loading, growth of these nucleated voids depend on the various parameters including, void volume fraction, stress triaxiality and the material characteristics of the matrix containing the void (Gurson, 1977; Rice and Tracey, 1969; Tvergaard and Needleman, 1984). After considerable growth of void, depending on the void volume fraction, void coalescence starts and forms a crack which propagates ultimately leading to failure (Gurson, 1977; Rice and Tracey, 1969; Tvergaard and Needleman, 1984). A brief overview of the aspects discussed above is given below from a multiscale plasticity theory perspective.

Rice & Tracey (1969) applied the effect of void growth in the continuum isotropic plasticity scale in the context that void growth and coalescence were observed to be the dominant reason of ductile fracture. Gurson (1977) incorporated the mechanism of void nucleation and growth in ductile materials' yield function. A yield function was approximated using the macroscopic flow behaviour of simplified physical model of void in a rigid-perfectly plastic matrix bounded by the von Mises yield criterion. Huang (1991) introduced the effect of shape changing part of velocity field on void growth rate and modified the well-known relation given by Rice and Tracey. Fleck & Hutchinson (1993) first demonstrated the dependence of void size on porous ductile material behaviour using macroscale continuum plasticity. A strain gradient theory was incorporated to investigate the void size effect on the macroscopic softening of ductile materials. Extensions in the classical Gurson model have been made by various researchers, Gologanu et al. (1993) included provision for elliptical voids in the model, Leblond et al. (1995) incorporated hardening in the matrix surrounding the void, Gologanu et al. (1997) further accommodated inhomogeneous strain rate for the application of simulation of representative cell at a near crack tip region, Monchiet et al. (2007) studied the expression for the macroscopic criterion for oblate and prolate voids embedded in perfectly plastic rigid matrix. Monchiet & Bonnet (2013) presented a closed form expression of the macroscopic criterion in which the size effects of void were included in the classical Gurson model using the Fleck and Hutchinson strain gradient plasticity approach.

2

Tvergaard & Needleman (1984) modelled the deformation of round tensile bar necking and consequent failure. This model used macroscale isotropic elastic-plastic constitutive relations which includes behaviour of void nucleation and growth. This study laid down the ground work for the future numerical modelling of void nucleation and growth and is generally called GTN, Gurson-Tvergaard-Needleman model. Tvergaard (1989) describes the material failure by void coalescence of microscopic sized voids. Void coalescence was calculated and was attributed to the growth of nucleated voids to the order of their inter separation and consequent necking by slip, of the material between the voids. The effect of Lode parameter on the void growth and void shape with the help of unit cell ~~with~~ using isotropic elastoplastic material was studied by Zhang et al. (2001) and concluded that it has a strong influence of void growth and coalescence. Benzerga & Besson (2001) treated the matrix as an anisotropic plastic media rather than the rigid-perfectly plastic assumption of Gurson, containing void in it and presented a modified model. Liu et al. (2003) introduced the effect of initial void size on the void growth rate. Modification in Rice and Tracey exponential void growth model was suggested and made it dependent on the square of mean stress. Liu et al. (2005) introduced the effect of a shape changing part of the velocity field on the void growth into the model. Monchiet et al. (2008) investigated the combined effect of void shape and anisotropic nature of matrix in which void is embedded on the macroscopic response of porous ductile materials. The Gologanu–Leblond–Devaux's (GLD) model was extended to incorporate an anisotropic material that obeys the anisotropic yield criterion presented by Hill (1948). Benzerga & Leblond (2010) presented a comprehensive work on void nucleation, growth and its applications to material failure. It discussed experimental background, available models and their application in FEA along with macroscale viscoplastic modelling. Stewart & Cazacu (2011) incorporated the effects of material anisotropy, incompressibility, tension-compression asymmetry of matrix having void in it, into the available models to develop macroscopic yield criterion for a porous ductile material. Lode parameter effect and strain localisation in a band around void is studied using unit cell with spherical void by Barsoum and Faleskog (2011) and the importance of Lode parameter in ductile failure was emphasised. Nielsen and Tvergaard (2011) investigated the void growth in a unit cell with void with matrix having isotropic elastoplastic properties under shearing load and studied the shear band effect on void growth and coalescence. Danas and Ponte Castañeda, (2012) presented a macroscale homogenisation based model which incorporates the effect of stress triaxiality and Lode parameter on the void growth and evolution of void shape and orientation. Siddiq et al. (2012) included a variational void coalescence model in the porous constitutive model. Sayed et al. (2012) studied the combined effects of shape memory alloy plasticity and porous plasticity. Dunand and Mohr (2014) studied the localisation of plastic flow around void with unit cell simulation with Levy – von Mises matric material and its onset under different stress states considering shear loading and Lode parameter. Niordson and Kysar (2014) developed a strain gradient based crystal plasticity formulation and used void growth in FCC and HCP single crystals in 2D as a case study for the model. Zhou et al. (2014) combined the volumetric damage, which depends on a void volume fraction, and shear damage to improve the GTN model so that it can be effectively used to model damage in low stress triaxialities. Tekoğlu, Hutchinson and Pardoen (2015) also studied the effects of strain localisation on the void coalescence under different stress states using unit cell with void simulations. Siddiq & El Sayed (2015) included the effects of strain rate in the previously developed variational void coalescence model. Song and Castañeda (2017, 2017, 2018) presented a macroscale homogenisation-based constitutive model for porous polycrystalline material. Siddiq (2018) incorporated the effects of parameters including initial porosity, stress triaxiality and crystal orientation on the void growth and failure in a porous crystal plasticity constitutive model. Niordson and Tvergaard (2018) presented a macroscale constitutive model for porous polycrystals with strain gradient effects included in it. Void growth in shear bands under high shear stress state are studied using a macroscale isotropic continuum plasticity model accounting for void growth by Torki and

3

Benzerga (2018). In addition to the work mentioned above there has also been work where continuum damage modelling has been performed in the context of creep (Basirat et al., 2012; Besson, 2009), hydrogen effect (Fischer and Svoboda, 2014), stress-state dependent plasticity (Gao et al., 2011), void nucleation due to deformation localisation (Kadkhodapour et al., 2011), ductile damage at large strain (Lecarme est al., 2011, Li et al., 2011),   and the effect of void growth on overall plasticity using discrete dislocation dynamics (Basirat et al., 2012; Besson, 2009; Fischer and Svoboda, 2014; Gao et al., 2011; Kadkhodapour et al., 2011; Lecarme et al., 2011; Li et al., 2011; Segurado and LLorca, 2010).

O'Regan et al. (1997) carried out two dimensional (2D) plain strain study of void growth in a face centred cubic (FCC) single crystal using crystal plasticity and studied the effect of initial porosity, loading state and crystal orientation. Quinn et al. (1997) carried out the same study with hexagonal as well as circular voids. Orsini & Zikry (2001) carried out the same study with an array of voids in an FCC single crystal. A 2D plain strain study of void growth and coalescence under uniaxial and biaxial loading and various crystal orientation in a FCC single crystal modelled using 3D crystal plasticity was carried out by G.P. Potirniche et al. (2006). Liu et al. (2007) investigated void growth and coalescence at various crystal orientations in one and two spherical voids embedded in a 3D FCC single crystal with material matrix modelled using crystal plasticity. Size effects were incorporated in a 2D crystal plasticity model with three in-plane slip systems by Borg et al. (2008) and studied the void growth at biaxial loading at various initial porosity and crystal orientation . Yu et al. (2010) investigated the effects of stress triaxiality, initial porosity, Lode parameter, crystal orientation, activated slip and elastic anisotropy on the growth of spherical void in a BCC single crystal where matrix was modelled using crystal plasticity. Ha & Kim (2010) studied the same effects in an FCC single crystal. Yerra et al. (2010) studied the evolution of void shape and strain at the onset of void coalescence in a BCC single crystal on top of the parameters already studied by the previous researchers. Pushkareva et al. (2016) conducted representative volume element (RVE) study of multiple grains of commercially pure titanium. Deformation behaviour of one of the grain containing one and two voids was modelled using crystal plasticity theory incorporating slip whereas rest of the grains were modelled using J_2 plasticity. These simulations were carried out at uniaxial loading conditions. Asim et al. (2017) compared the void growth using local and non-local model in an FCC single crystal at high triaxialities. Various crystal orientations and initial porosity in spherical and ellipsoidal voids were investigated. Guo and Li, (2018) recently presented the crystal plasticity study of void growth in unit cell of BCC single crystal and extended the results to polycrystal application and compared the results with classical GTN model with conclusion that GTN model can be improved with information obtained by CP study. Savage *et al.*, (2018) conducted a unit cell study with BCC single and polycrystal having a spherical void in axisymmetric tension and compression cases to compare the results with the ones obtained from macroscopic analytical dilatational models for porous polycrystals.

There has been efforts in the past to study the void growth at the grain boundary with the grains having same crystal structure but different orientations. Li & Guo (2002) investigated the effect of isotropic macroscale plasticity parameter mismatch on the growth of void present at the interface of the bi-material matrices. Yang and Dong (2009) studied void growth in FCC single and bicrystals with different disorientations between the crystals and the void at the interface of the two grains. Jeong et al. (2018) studied void growth in a BCC single crystal and at the grain boundary of two BCC grains with different crystal orientations.

As discussed above, most of the work has been concentrated on FCC and BCC crystals and little effort has been made to study the effect of void growth in HCP single phase and almost no study on HCP-BCC bi-phase materials. This study presents one of the very few investigations of the void growth in an HCP single crystal of titanium alloy at higher stress triaxialities in a 3D RVE containing spherical

4

~~void,~~ using CPFEM framework~~, in an HCP single crystal of titanium alloy at higher stress triaxialities~~. ~~However, i~~It must be emphasized that there have been previous void growth studies using crystal plasticity on magnesium alloys which also has HCP crystal structure, but their application is limited by the fact that they have been carried out in 2D which loses complex effects of crystal orientation, void shape and orientation (Prasad et al., 2017, 2016; Thakare et al., 2009). Also, the plastic slip in HCP crystal structure has very limited symmetry and out of plane behaviour can prove to be crucial to make right estimation. In addition <u>the main novelty of the presented work is</u>~~,~~ <u>in the fact that</u> a very first study of void growth at the boundary of two dissimilar grains (BCC and HCP) is presented, a case which arises in α-β titanium alloys (Ti-10V-2Fe-3Al). The effects of the BOR, initial porosity and the phase boundary inclination (PBI) is studied. A matrix material for both the scenarios was modelled using a fully validated three-dimensional crystal plasticity finite element method (CPFEM).

2. Modelling Concept

2.1. Crystal plasticity theory

Crystal plasticity finite element method has been used in various other application areas (Alharbi and Kalidindi, 2015; Aoyagi et al., 2014; Barbe and Quey, 2011; Bridier et al., 2009; Choi et al., 2011; Erinosho and Dunne, 2015; Ghosh and Anahid, 2013; Gonzalez et al., 2014; Hansen et al., 2013; Herrera-Solaz et al., 2014; Khan and Liu, 2016; Kim et al., 2017; Kohar et al., 2017; Lim et al., 2015; Mayama et al., 2011; Mayeur et al., 2015; Popova et al., 2015; Siddiq et al., 2008, 2007; Siddiq and El Sayed, 2011; Siddiq and Ghassemieh, 2008; Siddiq and Schmauder, 2006; Su et al., 2016; Upadhyay et al., 2018; Zhang et al., 2015, 2018) beside the ductile failure which is already discussed above. Details of which are not discussed here for brevity.

A brief overview of the crystal plasticity theory used during this work is presented below which is based on Marin (2006). Total deformation gradient is given by:

$$\boldsymbol{F} = \boldsymbol{V}^e \boldsymbol{F}^*, \ \ \boldsymbol{F}^* = \boldsymbol{R}^e \boldsymbol{F}^p \tag{1}$$

Here, the total deformation gradient, $\boldsymbol{F}$, is multiplicatively decomposed into an elastic stretch tensor, $\boldsymbol{V}^e$, and $\boldsymbol{F}^*$. $\boldsymbol{F}^*$ represents an intermediate configuration, $\widetilde{\boldsymbol{B}}$, which includes, plastic deformation gradient, $\boldsymbol{F}^p$ and rigid body rotation, $\boldsymbol{R}^e$. Furthermore, total velocity gradient, $\boldsymbol{l}$, can be calculated from $\boldsymbol{F}$ using:

$$\boldsymbol{l} = \dot{\boldsymbol{F}} \boldsymbol{F}^{-1} \tag{2}$$

Velocity gradient in $\widetilde{\boldsymbol{B}}$, $\tilde{\boldsymbol{L}}$, is given by:

$$\tilde{\boldsymbol{L}} = \boldsymbol{V}^{e-1} \boldsymbol{l} \boldsymbol{V}^e \tag{3}$$

Further decomposition of $\tilde{\boldsymbol{L}}$ into its symmetric and antisymmetric (skew) parts was carried out and the results are:

$$\widetilde{\boldsymbol{D}} = \boldsymbol{V}^{eT} \boldsymbol{d} \boldsymbol{V}^e = \dot{\widetilde{\boldsymbol{E}}}^e + \widetilde{\boldsymbol{D}}^* \tag{4}$$

$$\widehat{\boldsymbol{W}} = \boldsymbol{V}^{eT} \boldsymbol{w} \boldsymbol{V}^e = s\text{kew}(\boldsymbol{V}^{eT} \dot{\boldsymbol{V}}^e) + \widehat{\boldsymbol{W}}^* \tag{5}$$

Here $\boldsymbol{d}$ and $\boldsymbol{w}$ are symmetric and skewed parts of total velocity gradient respectively, given by $\boldsymbol{l} = \boldsymbol{d} + \boldsymbol{w}$. $\dot{\widetilde{\boldsymbol{E}}}^e$ is the rate of applied elastic strain, and $\widetilde{\boldsymbol{D}}^*$ and $\widehat{\boldsymbol{W}}^*$ are the symmetric and skewed parts of the plastic flow respectively, arising from crystallographic slip and lattice rotation.

Second Piola-Kirchhoff stress in $\widetilde{\boldsymbol{B}}$ configuration can be calculated using second order elasticity tensor, $\widetilde{\mathbb{C}}^e$, applied elastic strain.

$$\tilde{S} = \widetilde{\mathbb{C}}^e : \widetilde{\boldsymbol{E}}^e \tag{6}$$

5

The symmetric and skewed parts of plastic flow can be defined by the contributions from plastic slip and lattice rotation, the first and second terms in (7) and (8) respectively. Here $\widetilde{\boldsymbol{\Omega}}^e$ is the spin of lattice, given by $\widetilde{\boldsymbol{\Omega}}^e = \dot{\boldsymbol{R}}^e \boldsymbol{R}^{eT}$, $\widetilde{\boldsymbol{C}}^e$ is the elastic right Cauchy-Green tensors in $\widetilde{\boldsymbol{B}}$ configuration, given by $\widetilde{\boldsymbol{C}}^e = \boldsymbol{V}^{eT}\boldsymbol{V}^e$ and $\widetilde{\boldsymbol{Z}}^\alpha$ is the Schmid tensor of the α slip system in $\widetilde{\boldsymbol{B}}$ configuration.

$$\widetilde{\boldsymbol{D}}^* = \text{sym}\big(\widetilde{\boldsymbol{C}}^e \widetilde{\boldsymbol{\Omega}}^e\big) + \sum_{\alpha=1}^{N} \dot{\gamma}^\alpha \text{sym}\big(\widetilde{\boldsymbol{C}}^e \tilde{Z}^\alpha\big) \tag{7}$$

$$\widetilde{\boldsymbol{W}}^* = \text{skew}\big(\widetilde{\boldsymbol{C}}^e \widetilde{\boldsymbol{\Omega}}^e\big) + \sum_{\alpha=1}^{N} \dot{\gamma}^\alpha \text{skew}\big(\widetilde{\boldsymbol{C}}^e \tilde{Z}^\alpha\big) \tag{8}$$

Evolution of plastic shear strain rate of the α slip system, $\dot{\gamma}^\alpha$, is given in (9). This is a Taylor type power law flow rule where $\dot{\gamma}_0^\alpha$ is the reference shear rate, τ^α is the resolved shear stress on the α slip system, κ_s^α is the strength of the α slip system at that instance and m is the rate sensitivity exponent.

$$\dot{\gamma}^\alpha = \dot{\gamma}_0^\alpha \left[\frac{|\tau^\alpha|}{\kappa_s^\alpha}\right]^{\frac{1}{m}} sign(\tau^\alpha) \tag{9}$$

Strength of the slip system is not constant and evolves with the slip activity. It is assumed in the formulation that all slip systems in a family hardens at the same rate. And depends on the reference hardness h_0, current strength κ_s, initial slip system family strength $\kappa_{s,0}$, saturation strength $\kappa_{s,S}$ and sum of shear strain on all the slip systems.

$$\dot{\kappa}_s = h_0 \left(\frac{\kappa_{s,S} - \kappa_s}{\kappa_{s,S} - \kappa_{s,0}}\right) \sum_{\alpha=1}^{N} |\dot{\gamma}^\alpha| \tag{10}$$

Saturation strength is given by:

$$\kappa_{s,S} = \kappa_{s,S0} \left[\frac{\sum_\alpha |\dot{\gamma}^\alpha|}{\dot{\gamma}_{S0}}\right]^{m'} \tag{11}$$

where $\kappa_{s,S0}$, $\dot{\gamma}_{S0}$ and m' are material parameters.

This formulation is implemented as a user material subroutine (UMAT) in ABAQUS (Simulia, 2012) for two distinct materials in order to carry out the simulations on crystals of dissimilar phases.

2.2. Homogenisation Scheme and Model Calibration

In case of dual phase titanium alloys, phases can coexist in various volume fractions. The procedure followed by Raghunathan et al. (2007) was used to calibrate the properties of α and β phases of Ti-1023 alloy's single crystals. Raghunathan et al (2007) used elastic-plastic self-consistent (EPSC) model in their work. This model is used for modelling polycrystalline aggregate behaviour, where each grain in the aggregate is considered as an elliptical inclusion in a homogenised effective medium. Hence this scheme works by finding the instantaneous value of stiffness of each grain and then its contribution is added to the homogenised response of the aggregate using Eshelby's equivalent inclusion formalism. It was reported that the single crystal elastic constants (SECs) and critical resolved shear stress (CRSS) values are the significant parameters while volume fractions, texture and morphology are less significant in EPSC models (Raghunathan et al., 2007).

In the present study, the main focus was to model the behaviour of a single- and bi-crystals which are highly anisotropic in nature and their behaviour is drastically influenced by the crystal orientations, in addition to SECs and CRSS. Also, we are interested to investigate the effects of void growth at the interface of two distinct crystal structures having different material properties which were influenced by the phase volume fractions. RVEs were constructed to study the voids at the interface of the α-β

6

phases which has fixed BORs and hence depend on the morphology too. These points lead to the use of current formulation for the case of void growth in single and bicrystal of α-β titanium alloy. SECs identified in that study (Raghunathan et al., 2007) were directly used, while the plasticity parameters were to be identified.

Tensile test data was used from a study carried out on the same material (Chen et al., 2010). Chen et al. performed a tensile test at room temperature with a crosshead speed of 1mm/min and the material used was as-received Ti-1023 alloy followed by heat treatment at 700°C for the duration of 1 hour and then water quenched. Volume fractions obtained by this heat treatment were 40% α_p and 60% β phase (Shihong and Guiqin, 1990).

Twinning at room temperature is suppressed in Ti-1023 because a sufficient amount of aluminium is present (Williams et al., 2002). Stress induced martensitic transformation has been seen in the Ti-1023 while solution treatment around and above β-transus temperature was carried out followed by water quenching. Since the test results used for this study are of samples which were heat treated at much lower temperature (700°C) than β-transus temperature of Ti-1023 (805±5°C) (Chen et al., 2010), stress induced martensitic transformation was not reported by the authors. That is why only slip based deformation was considered in this study. Three families of slip systems, $\{110\}_\beta \langle 111 \rangle_\beta$, $\{112\}_\beta \langle 111 \rangle_\beta$ and $\{123\}_\beta \langle 111 \rangle_\beta$ in β phase with BCC crystal structure were considered. Also, three families of Three slip systems of the HCP crystal system namely Basal $\{0002\}_\alpha \langle 11\bar{2}0 \rangle_\alpha$, Prismatic $\{10\bar{1}0\}_\alpha \langle 11\bar{2}0 \rangle_\alpha$ and Pyramidal $\{11\bar{2}2\}_\alpha \langle 11\bar{2}3 \rangle_\alpha$ were used to model the deformation in a single crystal α-phase.

Since the tensile test data was of polycrystalline and dual phase material, two integrations points were used for calibration. Properties of α and β phases were assigned to each of the integration points and crystal orientations of 200 randomly oriented grains of each of the two phases were assigned to the respective integration point. Size of all grains were considered to be equal (Marin, 2006). Deformation boundary condition of uniaxial tension with suitably high value of $1/m$ in (9) was used to get rate independent response. Average values of Cauchy stress of each phase, Σ_α and Σ_β, were obtained using the stresses of each grain of each phase, $\sigma_{g,\alpha}$ and $\sigma_{g,\beta}$, using:

$$\Sigma_\alpha = \sum_{g=1}^{N} \frac{\sigma_{g,\alpha}}{N}, \qquad \Sigma_\beta = \sum_{g=1}^{N} \frac{\sigma_{g,\beta}}{N}$$

(12)

Here N is the number of grains used, which is kept at 200. The homogenised value of Cauchy stress of the two integration points (representing each of the phases), $\Sigma_{\alpha-\beta}$, to get the homogenised response of the dual phase alloy were calculated using (13)(13). The volume averaged response of the average stress values, Σ_α and Σ_β, was calculated using the phase volume fractions, which were v_α=0.4 for α phase and v_β=0.6 for β phase, using:

$$\Sigma_{\alpha-\beta} = v_\alpha \Sigma_\alpha + v_\beta \Sigma_\beta$$

(13)

Ratios of the values of CRSS used by Raghunathan et al. (2007) were maintained and then the values of CRSS were iteratively adjusted to match the experimental results from the literature. The same procedure for finding out the material parameters for the crystal plasticity formulation given above has been used by researchers in the past (Jeong et al., 2018; Kalidindi et al., 1992; Kalidindi and Anand, 1992; Kim et al., 2012; Kocks et al., 1989; Mathur and Dawson, 1989). Figure 1Figure 1 shows the comparison of experimental stress-strain data from the literature and the CPFEM results with the calibrated parameters. Table 1Table 1 summarises all the parameters identified and used in the current study. Parameter κ_0 is the CRSS, for each slip system when shear strains due to plastic slip are

zero. Rest of the parameters $\kappa_{s,0}$, $\kappa_{s,S0}$, h_0, $\dot{\gamma}_{S0}$ and m_s are material constants used in (10) and (11) for the update of CRSS, κ_s, with increase in accumulated slip using Voce type hardening law.
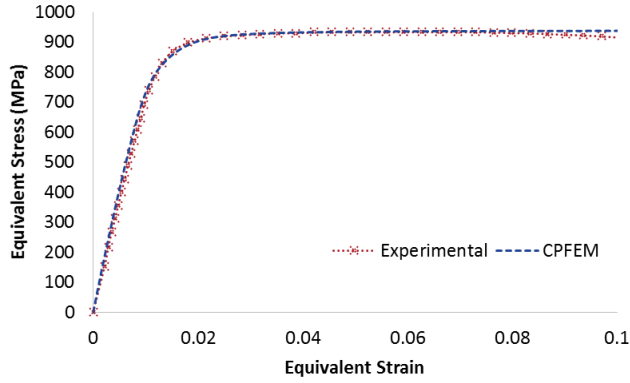

Figure 1: Model calibration with experimental results of Ti-1023 from the literature (Chen et al, 2010)

Table 1: Material parameters for CPFEM of Ti-1023 α-β phases

α phase Properties							
Elastic Properties	C11		C12		C13	C33	C44
(GPa)	163.0		114.0		69.3	191.0	38.0
Plastic Properties	$\dot{\gamma}_0$	m	h_0	κ_0	$\kappa_{s,0}$	$\kappa_{s,S0}$	$\dot{\gamma}_{S0}$	m_S
				(MPa)				
Basal	0.1	0.05	1	350	100	350	5×10^{10}	0.005
Prismatic	0.1	0.05	1	300	100	300	5×10^{10}	0.005
Pyramidal	0.1	0.05	1	750	100	750	5×10^{10}	0.005
β phase Properties							
Elastic Properties	C11		C12		C44		
(GPa)	140.0		128.0		50.0		
Plastic Properties	$\dot{\gamma}_0$	m	h_0	κ_0	$\kappa_{s,0}$	$\kappa_{s,S0}$	$\dot{\gamma}_{S0}$	m_S
				(MPa)				
$\{110\}\langle111\rangle$	0.1	0.05	1	285	100	285	5×10^{10}	0.005
$\{110\}\langle112\rangle$	0.1	0.05	1	320	100	320	5×10^{10}	0.005
$\{110\}\langle123\rangle$	0.1	0.05	1	380	100	380	5×10^{10}	0.005

2.3. RVE geometry and Boundary Conditions

Two different scenarios were studied, based on the possible nucleation sites of voids in α-β titanium alloy such as Ti-10V-2Fe-3Al. Terlinde et al. (1983) identified these void nucleation sites and are shown in Figure 2Figure 2 (a). The first scenario is of a void in α_p, primary alpha phase, which is essentially globular α phase in Ti-1023, labelled as '1' in Figure 2Figure 2 (a). The second scenario is of a void at α-β interface. This possible site is labelled '2' in Figure 2Figure 2 (a) where secondary alpha, α_s (shown as shaded region) is present in β matrix. Alternating α-β phases' lathes are present in many other α-β alloys as well and this study will be helpful to study their general behaviour.
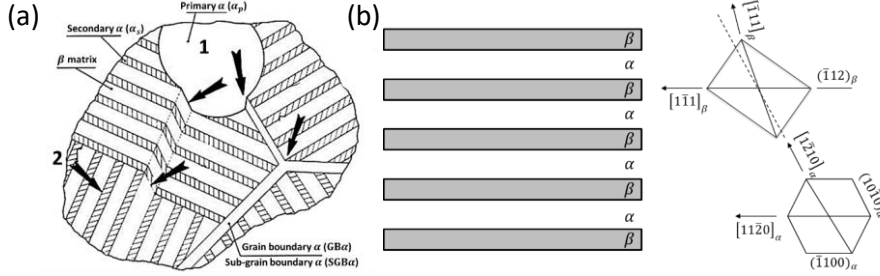
Figure 2: (a) Possible void nucleation Sites in Ti-1023 (Terlinde et al., 1983) (b) BOR between α-β phase lamellae

RVEs were made for each of these two scenarios. In the first scenario, a single spherical void was embedded in the centre of a cubic geometry. Matrix of this RVE is assigned the properties from Table 1~~Table 1~~ of the α phase (HCP) single crystal which were found using the procedure outlined in Section 2.2~~2.2~~. Two different initial porosities (f_0=0.001 and 0.01) were investigated. Figure 3~~Figure 3~~ (a) shows a half of the geometry with f_0=0.01.

Two different initial single crystal orientations (Ori 1 & 2) were tested for each of the two initial porosities (0.001 and 0.01). Their Euler angles for these orientations are given in Table 2~~Table 2~~. All these geometries were subjected to triaxial loading. Stress triaxiality (X) and the Lode parameter (L) were kept constant using multipoint constraint (MPC) throughout the loading, and are given by:

$$X = \frac{\Sigma_H}{3\Sigma_e} \tag{14}$$

$$L = \frac{2\Sigma_{II} - \Sigma_I - \Sigma_{III}}{\Sigma_I - \Sigma_{III}} \tag{15}$$

where Σ_H and Σ_e are the volumetric and equivalent stresses of the RVE and Σ_I, Σ_{II} and Σ_{III} are the first second and third principal stresses of the RVE.

The MPC was applied as an ABAQUS user subroutine. Investigations were carried out at different levels of stress triaxiality ranging from, 1/3 (uniaxial), to 3 (crack tip) and at $L = -1$ which is axisymmetric case with one tensile and two compressive stress components. At a stress triaxiality of 1, $L = 0$ which is a case of in-plane shear with one stress component equal to zero (for example in the case of plane-stress), and $L = 1$ which is also an axisymmetric case but in this case two stress components are tensile and one is compressive as is the case with biaxial tension, are also tested in addition to $L = -1$. Methodology proposed by Tekoglu (2014) was used to keep the stress triaxiality and the Lode parameter constant. Details are not given here for brevity.

Table 2: Crystal orientations used in single crystal (α-phase) study

Euler Angles	ψ	θ	ϕ
Ori 1	13.58°	153.68°	314.40°
Ori 2	346.98°	88.58°	325.61°

The Second scenario was realised by dividing the RVE into two halves and assigning the properties of the α-phase to one half and the β-phase to the other half which were found in section 2.2~~2.2~~. α-β phases are present as alternating lamellae as shown in Figure 2~~Figure 2~~ (b). BOR is not random between the two phases. Various researchers carried out experiments to identify the BOR between α-β phases. It was found that close-packed directions of the two crystals, $\langle 111 \rangle_\beta$ and $\langle 11\bar{2}0 \rangle_\alpha$, are aligned with little deviation (0.7°) (Bhattacharyya et al., 2003; Suri et al., 1999). There are 12 variants of BOR between α-β grains shown in Table 3~~Table 3~~. It is essentially the 12 possible $\{110\}_\beta \langle 111 \rangle_\beta$

slip systems aligned with $(0001)_\alpha\ [2\bar{1}\bar{1}0]_\alpha$. Since these slip systems have same strengths it was assumed initially that the void growth will not be affected by the choice of BOR variant. All 12 BOR variants were tested at stress triaxiality of 1 and initial porosity of 0.01 to verify this hypothesis. Phase boundary is the plane dividing phases. Phase boundary inclination, PBI, is defined here as the angle between the normal of the phase boundary (N) and the major loading direction (F), see Figure 3Figure 3 (d-g). BOR between α-β phases dictates that basal plane of HCP remain parallel to phase boundary, but one of the six possible closed packed planes of BCC can be aligned with phase boundary. Four different PBIs were modelled by rotating the phase boundary from 90° in PBI 1 to 0° in PBI 4 with decrements of 30°, with respect to the major loading axis (F), as shown in Figure 3Figure 3 (d-g). Table 4Table 4 gives the angle between major loading direction and normal to the phase boundary for the PBIs used. BOR variant 4 is used for all PBIs. In these cases, two initial porosities were investigated, f_0=0.001 (Figure 3Figure 3 (c (i) and (ii)), split in two halves for PBI 2) and 0.01 (Figure 3Figure 3 (b), shown for PBI 1). Again, all these geometries were tested at various levels of stress triaxialities.

Table   5
all the cases of bicrystals.
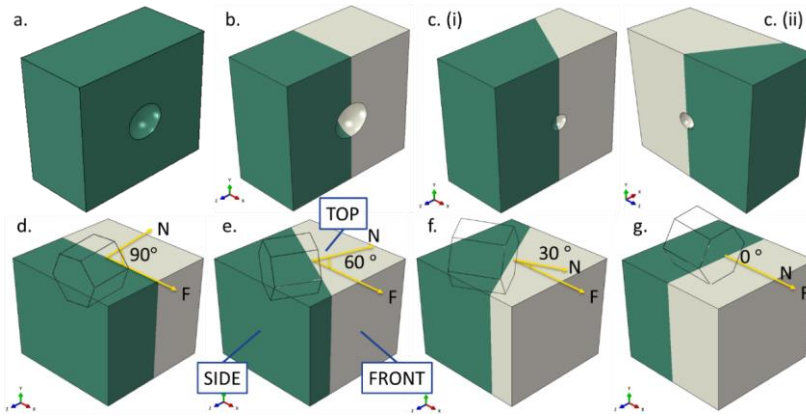
Figure 3: Geometries used in the simulations of Case 1 a) f_0=0.01, and Case 2 b) PBI 1, f_0=0.01, c) Halves of PBI 2, f_0=0.001, d)PBI 1, e) PBI 2, f) PBI 3, g) PBI 4. Here α-phase is green and β-phase in beige

Table 3: α-β phases BOR variants in Titanium alloys (Roy et al., 2012)

Variant No.	Corresponding plane	Corresponding direction
1	$(011)_\beta\|\|(0001)_\alpha$	$[\bar{1}\bar{1}1]_\beta\|\|[2\bar{1}\bar{1}0]_\alpha$
2		$[1\bar{1}1]_\beta\|\|[2\bar{1}\bar{1}0]_\alpha$
3	$(\bar{1}01)_\beta\|\|(0001)_\alpha$	$[1\bar{1}1]_\beta\|\|[2\bar{1}\bar{1}0]_\alpha$
4		$[111]_\beta\|\|[2\bar{1}\bar{1}0]_\alpha$
5	$(0\bar{1}1)_\beta\|\|(0001)_\alpha$	$[111]_\beta\|\|[2\bar{1}\bar{1}0]_\alpha$
6		$[\bar{1}11]_\beta\|\|[2\bar{1}\bar{1}0]_\alpha$
7	$(101)_\beta\|\|(0001)_\alpha$	$[\bar{1}11]_\beta\|\|[2\bar{1}\bar{1}0]_\alpha$
8		$[\bar{1}\bar{1}1]_\beta\|\|[2\bar{1}\bar{1}0]_\alpha$
9	$(\bar{1}10)_\beta\|\|(0001)_\alpha$	$[\bar{1}\bar{1}1]_\beta\|\|[2\bar{1}\bar{1}0]_\alpha$
10		$[111]_\beta\|\|[2\bar{1}\bar{1}0]_\alpha$
11	$(110)_\beta\|\|(0001)_\alpha$	$[1\bar{1}1]_\beta\|\|[2\bar{1}\bar{1}0]_\alpha$
12		$[\bar{1}11]_\beta\|\|[2\bar{1}\bar{1}0]_\alpha$

Table 4: PBIs used in the study and the corresponding angles between the major loading direction and normal of the phase boundary

	PBI 1	PBI 2	PBI 3	PBI 4
Angle	90°	60°	30°	0°

Table 5: Cases investigated in this study

	Single crystal α-phase		Bicrystal α-β phase				
	Ori 1	Ori 2	PBI 1/ BOR 1	PBI 1/ BOR 2-12	PBI 2	PBI 3	PBI 4
Lode Par.	-1, 0, 1				-1		
f_0	0.01 - 0.001	0.01 - 0.001	0.01 - 0.001	0.01	0.01 - 0.001	0.01 - 0.001	0.01 - 0.001
Triaxiality 1/3	x	x	x		x	x	x
1	x	x	x	x	x	x	x
2	x	x	x		x	x	x
3	x	x	x		x	x	x

3. Results and Discussion

3.1. Single crystal (α-phase)

3.1.1. The effect of initial porosity (f_0) on void growth in the α-phase single crystal

Figure 4Figure 4 (a) shows the evolution of void volume fraction (VVF) of two different initial porosities f_0, at stress triaxialities (X) of 1, 2 and 3, at Ori 1, normalised with initial VVF (f_0) using:

$$Normalised\ VVF = \frac{VVF}{f_0}$$

(16)

It can be inferred that for both values of f_0 and for all stress triaxialities, the normalised VVF increases exponentially with applied equivalent strain. Void growth rate increases exponentially with the increase in applied stress triaxiality. In the case of X=1, it increases exponentially initially then the rate slows down because the matrix material starts to undergo plastic deformation which dissipates the energy resulting in lower void growth. It can also be seen that as f_0 increases, the void growth slows down at higher stress triaxialities. While, at lower stress triaxialities void growth rate appears to have no significant difference. Results are consistent with the findings of the earlier researchers (Asim et al., 2017; Ha and Kim, 2010; Potirniche et al., 2006; Shu, 1998). Void growth is governed by the volumetric stress, a higher value will lead to larger void growth and vice versa. Figure 5Figure 5 shows the effect of f_0 on volumetric stress – volumetric strain response of Ori 1 at X=2. It can be seen that f_0=0.01 have lower value of stress for the given initial crystal orientation.

Effect of initial porosity on equivalent stress – equivalent strain response for Ori 1 at three stress triaxialities is shown in Figure 4Figure 4 (b). The values of equivalent stress are normalised using σ_0, highest value of yield stress among all the cases, so that comparison can be easily made between them. It can be seen that the values of yielding stress decreased with increase in the values of stress triaxialities. Since this is the combined response of the void and the matrix material in RVEs, decrease in yield stress followed by material softening was observed due to void growth. Higher softening was observed as the values of stress triaxialities were increase due to larger void growth. f_0=0.01 case experienced larger decrease in yielding stress with increasing stress triaxialities. On the contrary, f_0=0.001 led to lower reduction in yield stress with increasing stress triaxiality. This is because the increase in absolute value of porosity with void growth will be larger in f_0=0.01 case as compared to

11

f_0=0.001. Increase in the absolute value of VVF is higher in the case of higher initial porosities as compared to f_0=0.001 that is why the softening due to the increase in normalised VVF will be higher in case of f_0=0.01. Similar trends were observed for Ori 2.
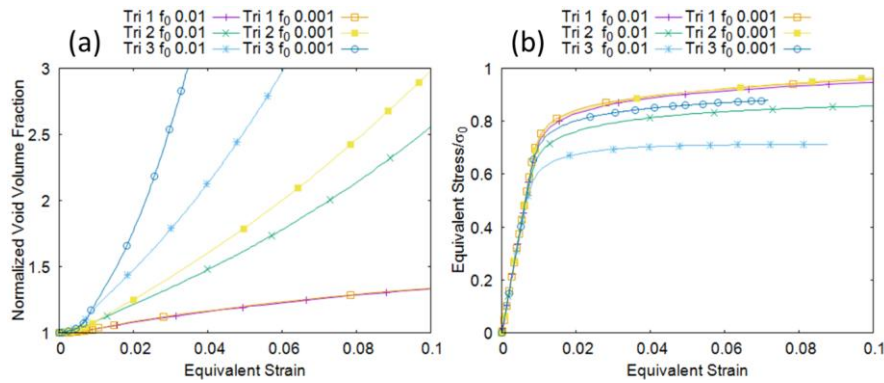

Figure 4: Effect of initial porosity, f_0 on (a) evolution of void volume fraction at initial crystal orientation Ori 1, and (b) equivalent stress- equivalent strain response at Ori 1 (σ_0= 1100 MPa)
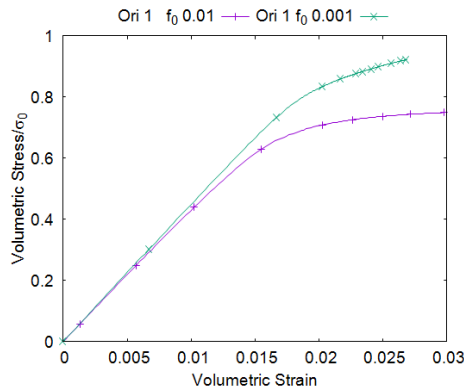

Figure 5: Effect of initial porosity, f_0 on volumetric stress –volumetric strain response of RVEs with initial crystal orientation Ori 1, X = 2 (σ_0=2500 MPa)

3.1.2. The effect of initial crystal orientation on void growth in the α-phase single crystal

Two random orientations of crystal lattice with respect to the loading axis were tested to investigate the effect of crystal orientation on void growth. These two orientations are shown in Figure 6Figure 6, in which *XYZ* is the global coordinate system and major loading is applied along the X-axis.

Figure 7 (a) compares void growth in terms of the normalized VVF with increasing equivalent strain in two RVEs with the Ori 1 and Ori 2, having initial porosity of f_0= 0.01. Void growth is compared at X= 1, 2 and 3. It can be observed that void growth is less in Ori 1 at all the values of stress triaxialities. As shown in Figure 8Figure 8 the value of volumetric stress in Ori 2 is higher than that of Ori 1 for same applied stress triaxiality. This led to higher void growth in Ori 2 than Ori 1.
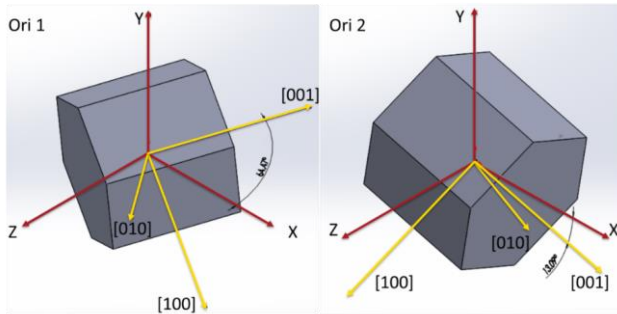
Figure 6: Visualization of the initial crystal orientations of α-phase single crystal with respect to the global coordinates used for RVE simulation
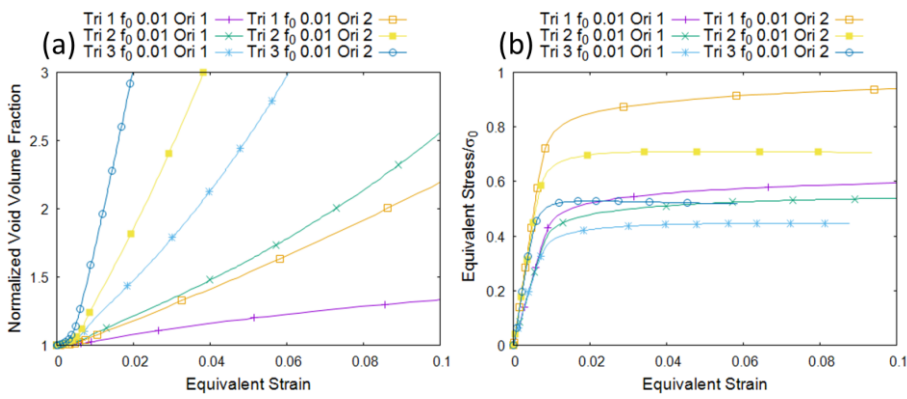
Figure 7: Effect of initial crystal orientation on evolution of VVF (a) and on equivalent stress- equivalent strain response (b) at f_0=0.01 (σ_0= 1750 MPa)
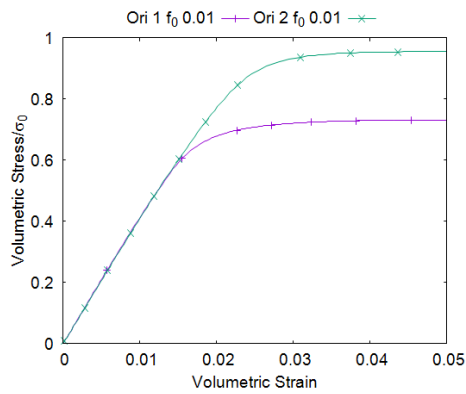

Figure 8: Effect of initial crystal orientation on volumetric stress –volumetric strain response of RVEs with f_0=0.01 and X = 2 (σ_0=2600 MPa)

The slip activity in the two cases were found to be different because different crystal orientations led to different Schmid factors. Higher slip activity resulted in higher plastic deformation in the matrix

13

material around the void because of higher void growth. The sum of shear strain due to slip from each slip system, γ^α, is termed as total shear strain, γ^{Tot}, which is given by:

$$\gamma^{Tot} = \gamma_n^{Tot} + \sum_{\alpha=1}^{N} \dot{\gamma}^\alpha \Delta t$$

(17)

Here $\dot{\gamma}^\alpha$ is the shear strain rate of slip system α. Contour plots of γ^{Tot}, which was saved as a solution dependent variable (SDV) are shown in Figure 9Figure 9 for these two different orientations. Plots are shown only for the cases of f_0=0.01, X=1, at an equivalent strain of 0.5 for brevity. The magnitudes of γ^{Tot} in the matrix region, away from outer edges and the void is larger in Ori 2 as compared to Ori 1, which signifies large overall plastic deformation in Ori 2. This leads to larger void growth, which can be seen by the larger value of γ^{Tot} near the void surface in Ori 2. This higher value of plastic deformation is attributed to the larger slip activity in Ori 2 as compared to Ori 1. Figure 10Figure 10 (a) and (b) show contour plots of γ^α for Ori 1 and Ori 2 respectively, for the same cases as Figure 9Figure 9. In Figure 10Figure 10, a1-a3 are for 3 Basal slip systems, a4-a6 are for 3 Prismatic slip systems and a7-a12 are for 6 Pyramidal slip systems for Ori 1, similarly with index b represents the same for Ori 2. It can be seen that the slip activity is considerably higher in Ori 2 for all slip systems. The slip activations in Ori 1 is comparatively smaller than Ori 2 for all slip systems so much so that it is almost non-existent in Pyramidal system.
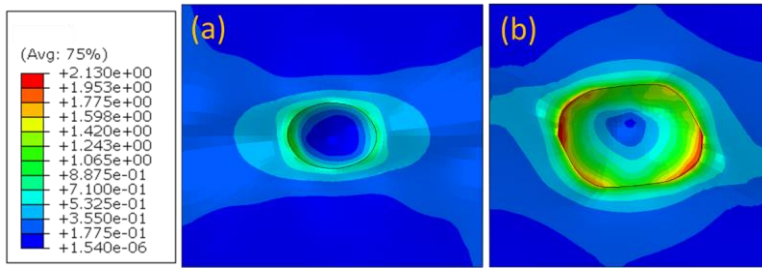
Figure 9: Contour plots of total shear strain (γ^{Tot}) due to slip in (a) Ori 1 and (b) Ori 2 at X=1, f_0=0.01 and ϵ_{eq}=0.5
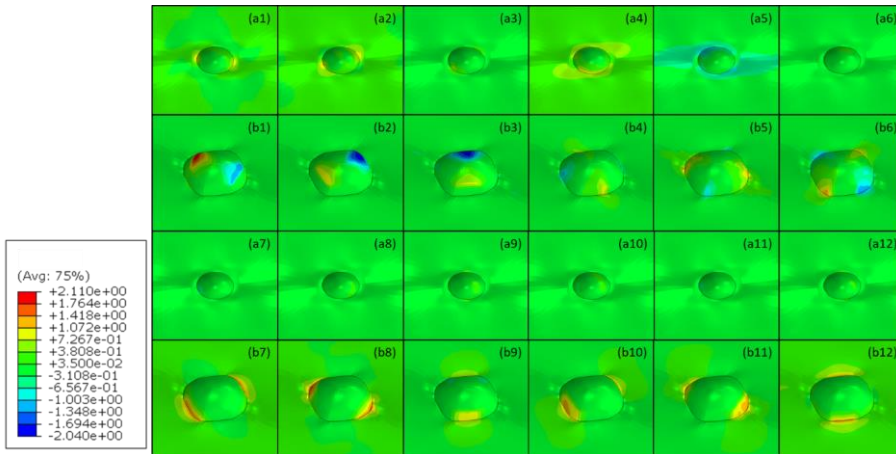

Figure 10: Contour plots of shear strain (γ^α) in each of the 12 slip systems in Ori 1 (a1-a3, Basal, a4-a6 Prismatic, a7-a12 Pyramidal) and Ori 2 (b1-b3, Basal, b4-b6 Prismatic, b7-b12 Pyramidal) in at X=1, f_0=0.01 and ϵ_{eq}=0.5

Since the HCP crystal system are low symmetry and highly anisotropic, there can be a high variation in their strengths. Equivalent stress – equivalent strain response of non-porous single crystals with the same crystal orientations as used in this study was~~is~~ given in ~~Figure 11~~Figure 11 for comparison and estimation of the difference between strengths. It can be seen that there is almost a twofold difference in yield stress and the modulus for Ori 1 both are quite low. This difference can also be seen in the equivalent stress – equivalent strain response of RVEs with Ori 1 and Ori 2 at different X and f_0=0.01 shown in Figure 7 (b). Same trends in yield stress and modulus seen in non-porous single crystals can be observed in case of RVEs with void. RVE with Ori 2 has higher yield strength at all stress triaxialities in comparison with Ori 1. But the amount of softening because of void growth is higher in Ori 2 when the triaxiality was increased, as compared to Ori 1. This is because of the higher rate of void growth in Ori 2 as compared to Ori 1 as was seen in Figure 7 (a). These results are consistent with the findings of other researchers, who performed similar studies on BCC single crystals, where the orientations with higher strength undergoes higher void growth and as a result soften more (Yerra et al., 2010).
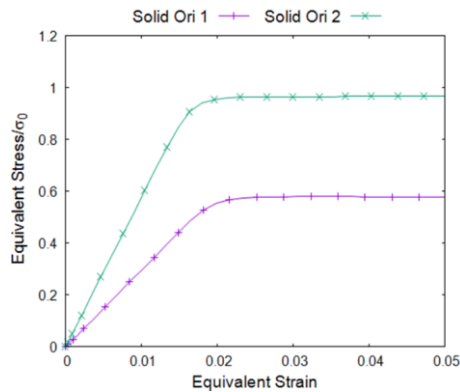
Figure 11: Effect of initial crystal orientation on equivalent stress – equivalent strain response on non-porous single crystal with uniaxial tensile loading and σ_0=1750 MPa

3.1.3. The effect of initial crystal orientation on final void shape and orientation in the α-phase single crystal

Spherical void shape was used in all the cases investigated in this study. Shape and orientation of the void evolved with the increase in applied loading on the RVE. Figure 12~~Figure 12~~ (a) shows the cross sections of void shape taken at three mutually perpendicular planes for Ori 1, f_0=0.01 at X=3. Here direction 1 is the major loading axis. Cross sections are shown at increments of 0.01 global value of equivalent strain from 0.00 to 0.05. Point at which the void axes length was calculated is marked. ''*' sign shows the maximum length at that strain and the 'X' shows the minimum length. ~~Evolution of axes lengths of void,~~Evolution of axes lengths of void normalised by the initial value against global equivalent strains for Ori 1 are given in Figure 13~~Figure 13~~ (a). It is found that the largest increase in size is along axis 1, whereas it decreased along axis 2 and remained almost constant along axis 3. This is because of the highly anisotropic nature of crystal due to which the deformation along three axes of RVE were found to be quite different even though constant stress triaxiality was imposed. Figure 12~~Figure 12~~ (b) shows the cross section of void in Ori 2, f_0=0.01 at X=3 at same equivalent strain increments. Figure 13~~Figure 13~~ (b) shows the lengths of the three axes of the voids. It can be inferred that the length along all three axes of void increased for this crystal orientation. Length along the major loading axis was maximum for this orientation as well. Also the shape of the void was like a skewed hexagon on 1-2 and 2-3 plane. Similar void shape has been reported in literature for other material having HCP crystal structure (Tang et al.,

2010). This is because of the slip activity on the surface of the void as shown in Figure 11Figure 11 (b1-b12). It can be seen that the magnitude of γ^α for pyramidal systems is higher in the orientations 60° apart from each other on the opposite sides of the void possibly giving rise to the hexagonal shape.
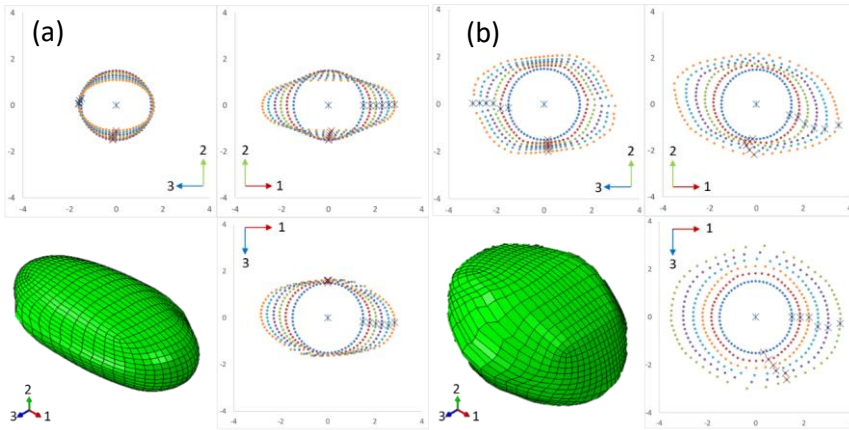

Figure 12: Shape of the voids in Ori 1 (a) and Ori 2 (b). Cross section views of the voids on X, Y and Z global planes are shown at RVE equivalent strain values of 0.00 (shown in blue) - 0.05 (shown in orange) for f_0 = 0.01 and X = 3 with the isometric view at 0.05 equivalent strain.
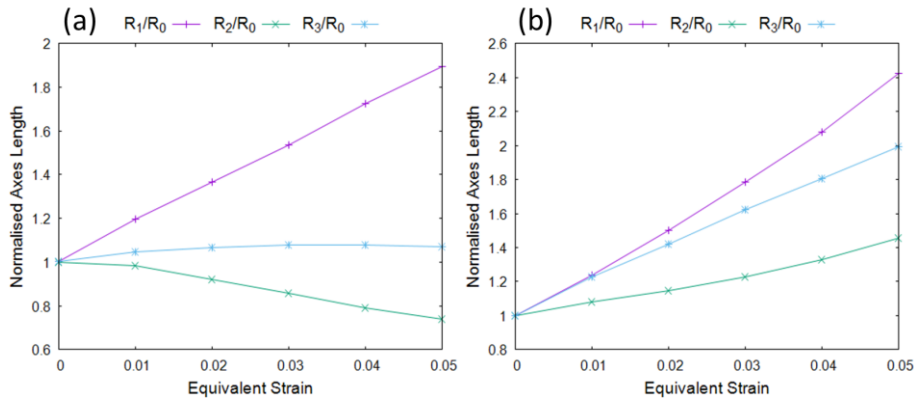
Figure 13: Evolution of the size of the voids in Ori 1 (a) and Ori 2 (b) with equivalent strain for f_0 = 0.01 and X = 3

It can also be seen in Figure 12Figure 12 (a) that there is slight rotation about all three axes as all the '*' and 'X' signs were not aligned for Ori 1. Maximum rotation was found to be about axis 2, shown on 1-3 plane. It first went clockwise then reversed the direction. In case of Ori 2, there is significant rotation of major axis of void about axis 3, as can be seen in 1-2 plane. Rotation was attribute to the fact that the lattice of crystal rotates as the deformation progresses due to slip. Since the matrix material around the void was undergoing higher plastic deformation due to slip, orientation of the lattice around void changes as well. This reorients the slip geometry which changes the deformation direction. Figure 14Figure 14 (a) and (b) gives the stereographic projections of the slip planes in Ori 1 and Ori 2 respectively. Orientation of the element undergoing maximum plastic deformation in each of the two cases were used. Three slip planes families, $\langle 0001 \rangle$, $\langle \bar{1}100 \rangle$ and $\langle 11\bar{2}2 \rangle$ were plotted at

same values of equivalent strains used in previous figure. Arrows shows the direction in which rotation progressed for each of the plane. Figure 15Figure 15 (a) and (b) give a better visualisation of orientation of crystal orientation in the element in going from equivalent strain 0 to 0.05 in Ori 1 and Ori 2 respectively.
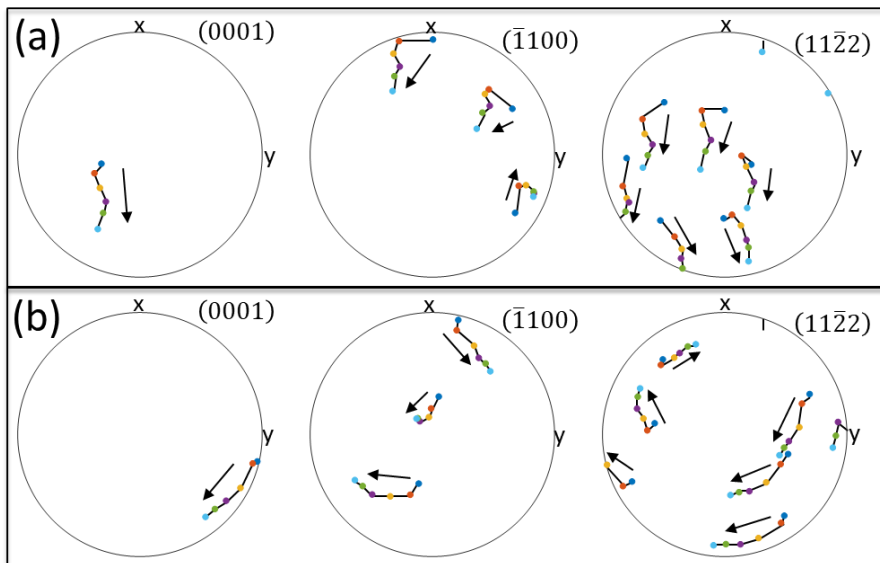

Figure 14: Stereographic projections of slip planes (0001), $(\bar{1}100)$ and $(11\bar{2}2)$ in upper hemisphere for an element of RVE in Ori 1 (a) and Ori 2 (b) for equivalent strain values of 0.00-0.05, f_0=0.01 and X=3. Arrows show the direction of rotations of planes with increasing strains
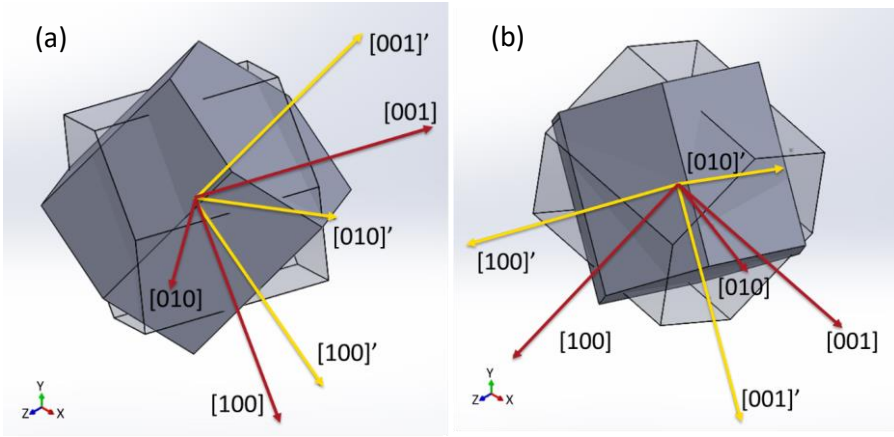
Figure 15: Crystal orientation of an element of RVE with Ori 1 (a) and Ori 2 (b) for equivalent strain values of 0.00 (translucent) and 0.05 (solid), f_0=0.01 and X=3

3.1.4. The effect of Lode parameter on void growth in the α-phase single crystal

The Lode parameter affects the void growth in single crystals as well as it does for the case of polycrystals (Barsoum and Faleskog, 2011; Kiran and Khandelwal, 2014; Tekoğlu et al., 2015; Zhang et al., 2001). In the present study, the effect of the Lode parameter is investigated for single crystal α phase. The normalised void volume fraction is plotted against equivalent strain of the two crystal orientations, Ori 1 and Ori 2 with $f_0 = 0.01$, at moderately high stress triaxiality, X=1 in Figure 16Figure 16 (a). It can be inferred from Figure 16Figure 16 (a) that the void growth slows down as the Lode parameter was increased from -1 to 1 for different crystal orientations. It was also observed that the reduction in void growth rate is higher in stronger crystal orientation, Ori 2, as compared to Ori 1. A deviation was observed in this trend in the case of Ori 1 L=1 where the void growth is initially slower than L= -1 and 0, but then increases exponentially and becomes higher than either of the two cases. This is attributed to the difference in slip activity in each of these cases which led to difference in strengths of the crystal and consequently resulted in higher void growth in L=1 case. The link between slip activity, strength of crystals and void growth will be established in the following. These results show that the effect of the Lode parameter is highly dependent on crystal orientation.

Single crystals are highly anisotropic and behave differently under different loading conditions. Equivalent stress-equivalent strain response for the above cases is plotted in Figure 16Figure 16 (b). It can be inferred from Figure 16Figure 16 (b) that there is a difference in yield strengths for different values of Lode parameter while having the same value of stress triaxiality and crystal orientation. In the case of Ori 2, difference between yield stress was found to be double between $L = -1$ and $L = 1$. On the other hand, difference in yield strengths for different Lode parameters is very small in the case of Ori 1. As it was discussed in earlier sections that a crystal with higher strength leads to higher volumetric stress for the same stress triaxiality which leads to higher void growth and a concentrated plastic deformation around void. Same phenomenon was observed in the cases of different Lode parameters. For the case of $L = -1$ strength of the crystal with Ori 2 is highest as can be seen in Figure 16Figure 16 (b) which led to highest void growth as shown in Figure 16Figure 16 (a). Similarly, a decrease in strength with an increase in the Lode parameter was observed which led to lower void growth.

18

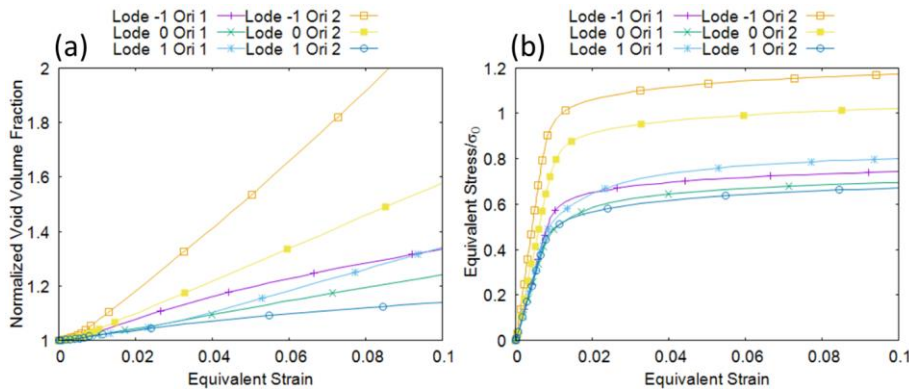*Figure 16: Effect of Lode parameter on (a) evolution of void volume fraction, and (b) equivalent stress- equivalent strain response at Ori 1 and 2, X=1, f_0=0.01 (σ_0= 1400 MPa)*

The accumulated shear strain due to slip, γ^{Tot}, in the matrix material is plotted for the case of Ori 1 in Figure 17Figure 17 (a-c) and for Ori 2 in Figure 17Figure 17 (d-f), each of which are at L=-1, 0 and 1, respectively. It can be seen inferred that the maximum amount of plastic deformation due to slip has occurred in the case of Ori 2, $L = -1$ (Figure 17Figure 17 (d)), which has undergone highest void growth. In this case, plastic deformation in the matrix material away formfrom the void is negligible. Whereas in the case of Ori 2, $L = 1$ (Figure 17Figure 17 (f)), the maximum value of plastic deformation in matrix material around void is almost one-third of that of $L = -1$. Also, some plastic deformation has occurred in the matrix material away from the void, making two diagonal bands, one of which is stronger than the other. These bands lead to energy dissipation by plastic deformation of the matrix rather than in void growth resulting in lower void growth in this case. In the case of Ori 1, difference in slip activity around void is not significant between the three values of the Lode parameter which was reflected in the results presented in Figure 16Figure 16 (a). In the cases of L=0 and 1 (Figure 17Figure 17 (b, c)), matrix material is undergoing plastic deformation which dissipates the energy resulting in lower void growth. These findings further elucidate the importance of void growth study at crystalline level since void growth in single crystals is a strong function of crystal orientations in addition to the loading conditions including stress triaxiality and Lode parameter.
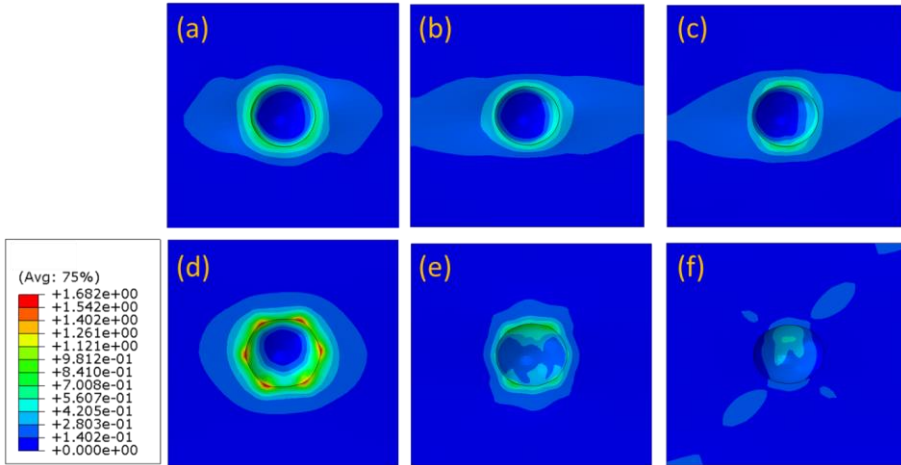
Figure 17: Contour plots of total shear strain (γ^{Tot}) due to slip in (a-c) Ori 1 and (d-f) Ori 2 for L=-1, 0 and 1, respectively, at X=1, f_0=0.01 and ϵ_{eq}=0.05

3.2. Bicrystal (α - β phases)

3.2.1. The effect of PBI on void growth in α - β phase bicrystal

The effect of phase boundary inclination (PBI) on void growth and equivalent stress – strain response was investigated at four different PBIs. Results are only shown for X= 1/3 and 3 for initial porosity, f_0 = 0.01. Figure 18 (a) shows evolution of void volume fraction for X=3.

It is found that in going from PBI 1 to 3, void growth rate is increasing. This effect is attributed to two different mechanisms which determine the rate of void growth.

1. Here refer to Figure 3~~Figure 3~~ (e) again where it can be seen that the Top face of the RVE, perpendicular to the plane in which, F, major loading direction and N, normal to the phase boundary, vectors are present is constrained to have same deformation in all 4 PBIs. Rest of the two faces, i.e. Front (perpendicular to the F) and Side (perpendicular to Top and Front face) are also constrained to remain straight for all PBIs but may not ensure same deformation in both phases for all PBIs. In case of PBI 1, the two phases are constraint to have same deformation along F at the Front face, whereas the Side face will deform depending upon relative stiffness of the two phases in that direction. But as the interface between the two phases were rotated beyond PBI 1 towards PBI 4, deformation in each phase along F cannot be constrained to be equal and will start to depend upon the relative stiffness of each phase. This effect will start to take effect slightly in case of PBI 2, increasing in PBI 3 and then completely takes over in PBI 4 as the interface become perpendicular to F. This is the first mechanism which governs the void growth in bicrystals studied.

2. The second mechanism is the one we have already established in case of single crystals that the crystal or crystal orientation with higher stiffness will lead to higher stress concentration around void and will undergo relatively higher void growth and vice versa (section 3.1.2~~3.1.2~~). In case of PBI 1 and PBI 2, α and β crystals are oriented such that β phase is stiffer than α phase as can be seen in Figure 19~~Figure 19~~ which shows the equivalent stress – strain response of α and β crystal in RVEs without void but having same PBI. It helps establish an estimate of the strength of each individual crystal in bicrystal.
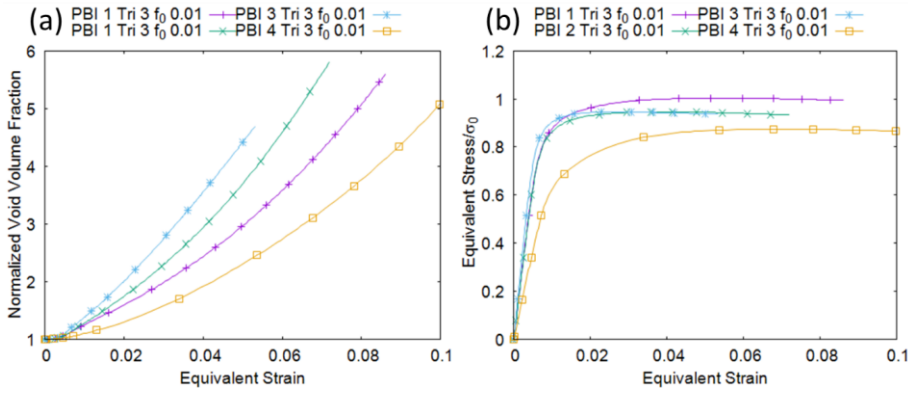
20

Figure 18: (a) Effect of PBI on evolution of void volumr fraction at X=3 with f_0=0.01, and (b) on equivalent stress-equivalent strain response with f_0=0.01, σ_0=664 MPa

In PBI 1 and 2 the two phases are either constraint to have same deformation along F (PBI 1) or major portion of them undergoes same deformation along F (PBI 2). In these cases, the second mechanism in which crystal orientation with higher strength undergoes higher void growth, takes over and void growth in β phase becomes higher than α phase because it was the stiffer crystal. This can be seen in Figure 20~~Figure 20~~ which shows the void shape and size at same values of global ϵ_{eq}=0.05 for X=3 and f_0=0.01. It shows the two views of voids for each PBI where view labelled 'Front' is the plane perpendicular to phase interface and Top face. Contours of γ^{Tot} are plotted on the surface of the void to show the amount of slip occurred due to void growth. Higher values of γ^{Tot} corresponds to higher slip activity.
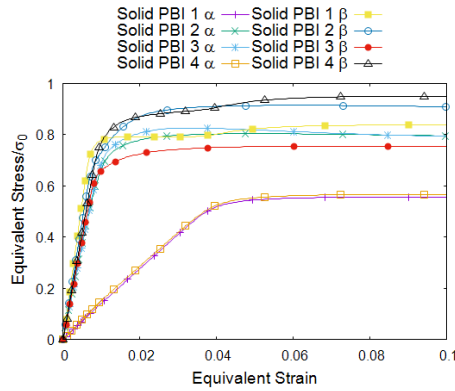

Figure 19: Effect of PBI on equivalent stress – equivalent strain response of bicrystal RVEs without void at X=3 (σ_0=1300 MPa)
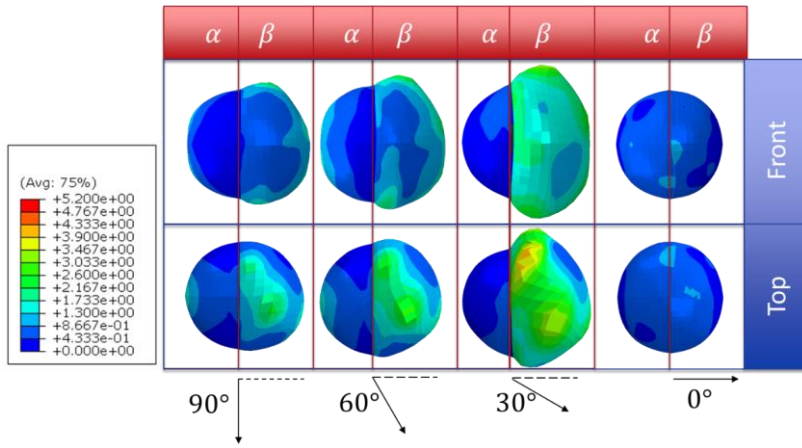
Figure 20: Shape of void with contours of γ_{Tot} for PBI 1 (90°), PBI 2 (60°), PBI 3 (30°) and PBI 4 (0°) for f_0=0.01, X=3 and ϵ_{eq}=0.05

Stiffness of β phase was further increased in PBI 2 which led to even higher total void growth due to higher void growth in β phase. Stiffness of β phase become lower than α phase in PBI 3 and lower than the values in PBI 1 and PBI 2 as can be seen in Figure 19Figure 19. In this case first mechanism becomes dominant where the deformation in two phases will depend upon their relative strengths. Since in PBI 3, phase interface is oriented such that the deformation along F will depend on relative stiffness of the two phases. And higher overall deformation will takes place in β phase since it is softer than α phase. Since the β matrix is undergoing higher deformation with triaxial loading condition, highest void growth was seen in PBI 3, so much so that the void in α phase grows only slightly (see Figure 20Figure 20). Stiffness of β phase becomes higher in PBI 4 due to its crystal orientation which makes deformation along F almost equal to α phase. Since Top and Side faces of the RVE are constrained to have same deformation in both phases in case of PBI 4, α phase did not deform as much in F direction although it has less stiffness than β phase. This in return retards the void growth in both phases and overall void growth becomes smaller than all the other PBIs. Comparison between the PBI 3 and 4 is made on the basis of slip activity in each of the two phases by plotting plastic slip γ^{α} for each slip system of α and β phases in Figure 21Figure 21. It can be seen that the slip in the β phase is higher than the α phase in PBI 3. In contrast, slip in the prismatic slip system in the α phase is comparable to slip in the β phase in PBI 4. And if the comparison is made between PBI 3 and PBI 4, slip in any of the slip system in PBI 4 is less than slip in PBI 3 due to less void growth in PBI 4.
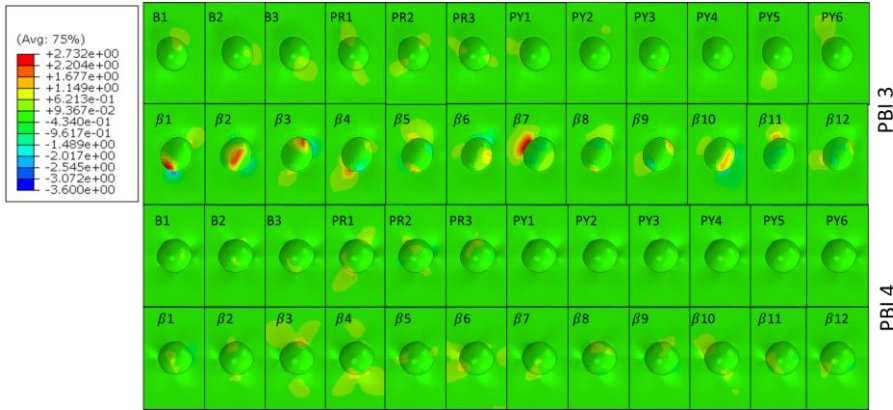
Figure 21: Contour plots of shear strain (γ^α) in each of the 12 slip systems in the α and β phases in PBI 3 and PBI 4, f_0=0.01 at X=3 and ϵ_{eq}=0.05. B, PR and PY stand for basal, prismatic and pyramidal respectively and β1-12 are 12 slip systems of $\langle 111 \rangle \{110\}$ family

Equivalent stress – strain response of each PBI at X=3 and f_0=0.01 is given in Figure 18 (b). It has been established previously (Section 3.1.2~~3.1.2~~) in case of single crystals that the configurations which have higher void growth will have larger drop in yield stress. Similar trend can be seen in case of bicrystals where yield stress in PBI 2 and PBI 3 is lower than PBI 1 because they have higher void growth than PBI 1. PBI 4 has the lowest value of yield stress because α phase in this PBI is the weakest of all other PBIs.

Figure 22 (a) shows the effect of PBI on void growth in the case of uniaxial loading. A similar trend was observed in this case as well where the void growth increases in going from PBI 1 to 4. There is an anomalous behaviour of void collapsing for all PBIs in uniaxial loading as can be seen in Figure 23~~Figure 23~~ (c) except in PBI 4. This happens because of a compressive loading in the β half to keep the lateral surfaces stress free and to keep the faces straight. Figure 23~~Figure 23~~ (a), (b) and (c) shows reaction force on the surfaces of RVE at ϵ_{eq}=0.01, 0.4 and 0.8 respectively. Each of these surfaces were constrained to remain stationary in the X, Y and Z directions. The α and β phase halves are marked in Figure 23~~Figure 23~~ (b). The void is also shown in each of these figures in red colour. The reaction force was anticipated to be maximum and negative on the face normal to the x-direction since the load was applied in the positive x-direction and negligible to zero on the transverse directions owing to uniaxial tensile loading. This holds true on the face normal to the z-direction. In the case of faces normal to the y-direction, loading is tensile in the α phase half, represented by arrows of the force acting downwards. But in the β half arrows are directed upwards on the bottom face and the void is collapsing. Since the two crystals have different stiffness due to the crystal structure and orientations, an extra loading appears on the Top surface of the RVE to keep the total stress equal to zero which is tensile in the α phase half and compressive β phase half. Same is true for PBI 2 where void in β phase half was compressed due to material stiffness mismatch. In case of PBI 3, this effect did not appear on the Top face but a compressive load on β phase half was present on the Side face. Due to the collapse of void in case of PBI 1 and 2 and retardation in void growth in PBI 3 the void growth rate decreased for all three PBIs in comparison with PBI 4. In PBI 4 void growth in α phase half was the major contributor in overall value of void growth and has tensile load in lateral directions which accelerated the growth. Because of this, void growth in PBI 4 was higher than PBI 1 and PBI 2, unlike in case of higher triaxiality case.

23

Equivalent stress – equivalent strain response for the case of uniaxial loading is shown Figure 22 (b) for f_0=0.01. Since the void growth in uniaxial case is not too high, the trend of increasing stiffness, in going from PBI 1 towards PBI 3 can be seen, but since the void growth in PBI 2 is higher than PBI 1, it appears to be softer than PBI 1. PBI 4 being the softest configuration and having higher void growth remain softest among all PBIs.
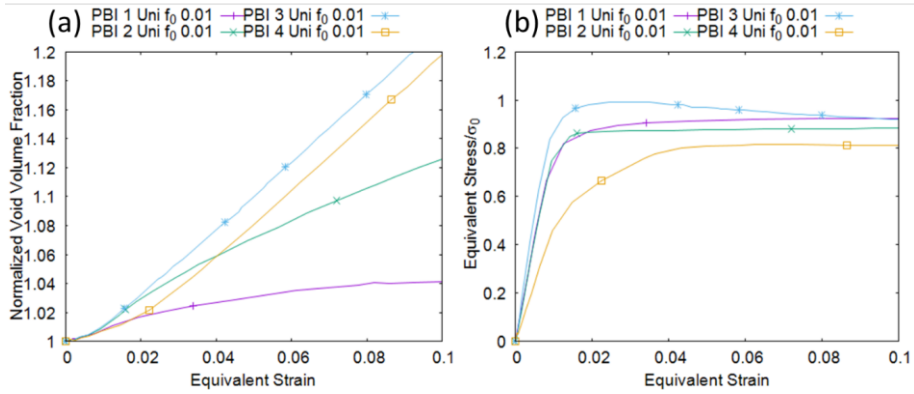

Figure 22: (a) Effect of PBI on evolution of void volume fraction at X=1/3 with f_0=0.01 and (b) on equivalent stress-equivalent strain response with f_0=0.01 (σ_0=960 MPa)
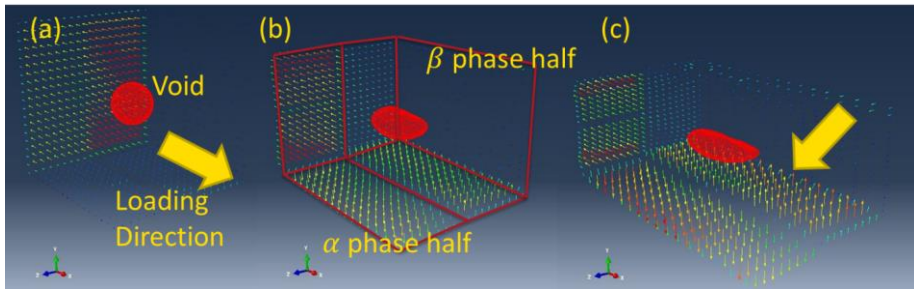

Figure 23: Void collapsing in β phase in case of uniaxial loading, f_0=0.01, ϵ_{eq}=0.01 (a), 0.4 (b) and 0.8 (c)

3.2.2. The effect of BOR variant on void growth in α-β phase bicrystal

All BOR variants mentioned in Table 3Table 3 were tested with PBI 1, f_0=0.01 and at X=1, and the results of void growth are shown in Figure 24 (a). It can be seen that there is a difference in void growth between the BOR variants. As discussed in section 2.32.3, these 12 BOR variants are 12 slip systems of $\{110\}_\beta \langle 111 \rangle_\beta$ family of β phase which are aligned with $(0001)_\alpha [2\bar{1}\bar{1}0]_\alpha$ slip system of α phase. It was expected that void growth and equivalent stress – equivalent strain response will not be affected by selection of BOR variant because of crystal symmetry. It was found in the simulation of RVEs without a void, that the equivalent stress – equivalent strain response is same for all BOR variants (results not shown here). But in case of RVEs with void, BOR variants were found to have different void growth rate and equivalent stress – equivalent strain response. Planes of $\{110\}_\beta$ family of β phase which are aligned with $[0001]_\alpha$ plane of α phase of BOR variants having same void growth are grouped together and shown in Figure 25Figure 25 (a), (b) and (c). BOR variants with same void growth were found to share the β phase interface planes which are 90° to each other about their intersection line.

24

Slip activity in the three distinct BOR variants 1, 3 and 9 is shown with the help of contour plots of γ^{Tot} on the planes passing at the midpoint of RVE in direction 1 and 2 shown in Figure 26Figure 26. Here direction 1 is parallel to major loading direction, F. It can be clearly seen that the slip activity in the BOR variants is not same and there is a distinct difference between the three. Amount of slip depends upon the Schmid factor and the stress concentration around the void. It can be seen that highest slip activity is found in case of BOR variant 3 followed by 1 and then 9. This is reflected in the void growth rate of the three variants.

Figure 24 (b) shows the equivalent stress – equivalent strain response of all the BOR variants. It can be seen that the BOR variants which have higher void growth are stiffer than the ones with lower void growth. Which is in agreement with the findings of void growth in single crystals presented in section 3.1.23.1.2 where faster void growth was observed in stronger crystal orientation.
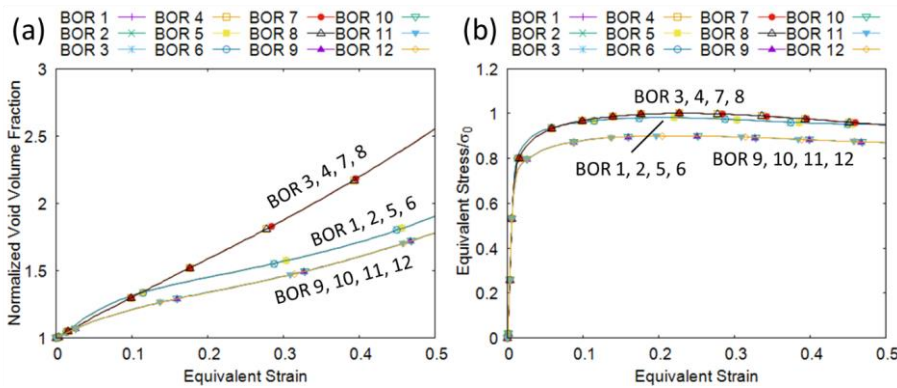

Figure 24: (a) Effect of BOR variant on evolution of VVF and (b) on equivalent stress – equivalent strain response with f_0= 0.01 and X=1 (σ_0=940 MPa)
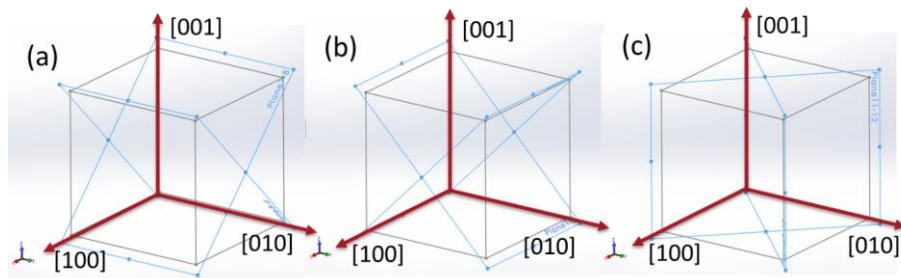

Figure 25: Planes of $\{100\}_\beta$ family aligned with $[0001]_\alpha$ plane of α phase for BOR 3, 4, 7 & 8 (a), BOR 1, 2, 5 & 6 (b), BOR 9, 10, 11 & 12 (c) shown on a BCC RVE
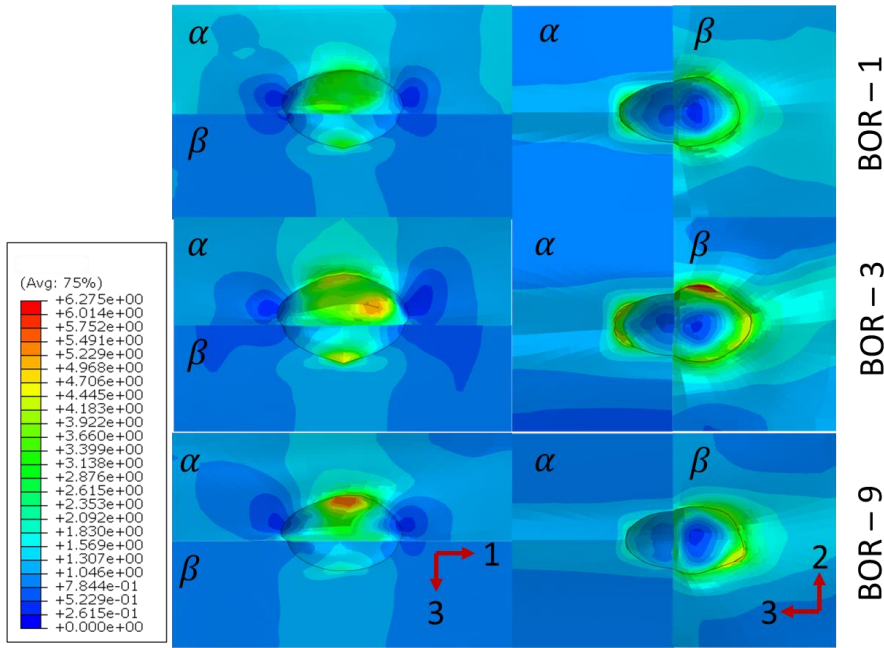
Figure 26: Contour plots of total shear strain (γ^{Tot}) due to slip in BOR variants with distinct void growth at X=1, f_0=0.01 and ϵ_{eq}=0.5

3.2.3. The effect of initial porosity on void growth in α-β phase bicrystal

The effect of initial porosity in the case of bicrystal simulations was found to be similar to the case of the single crystal. The void growth rate increased as the initial porosity was lowered from f_0=0.01 to 0.001 at higher stress triaxialities in all PBIs. Trends are plotted for all the four PBIs at two different f_0=0.01 and 0.001, at X=1/3 and 3 cases and shown in Figure 27 (a) and (c) respectively. In the uniaxial case shown in Figure 27 (a), trend observed in single crystal seems to be violated as in going from f_0=0.01 to 0.001 void growth rate in decreasing. Recalling the discussion of section ~~3.2.1~~3.2.1 there is a decrease in overall void growth in PBI 1, 2 and 3 because of compressive loading on β phase. In case of f_0=0.001 the collapse of void in β phase half increased even more because of higher compressive loading, which led to lower overall void growth. And as was observed in section ~~3.2.1~~3.2.1, PBI 4 do not have considerable compression of β phase half, void growth increased in case of f_0=0.001. Void growth in X=3 for f_0=0.001 and 0.01 for all PBIs is shown in Figure 27 (c). In case of higher stress triaxialities, trend observed in single crystal was repeated where decrease in initial porosity led to higher void growth rate for all PBIs because of the same reasons discussed in case of single crystal. Equivalent stress – strain response for uniaxial case, for all PBIs, for f_0=0.001 and 0.01 are shown in Figure 27 (b). It can be seen that the yield stress for f_0=0.001 is higher than 0.01 for all PBIs which is in agreement with the trends seen in single crystals. Same response can be seen in X=3 case in Figure 27 (d). All PBIs give stiffer response for f_0=0.001 as compared to 0.01. Higher softening is observed in case of f_0=0.01 since the actual void volume fraction increase in f_0=0.01 is higher than 0.001, as discussed in section ~~3.1.1~~3.1.1.
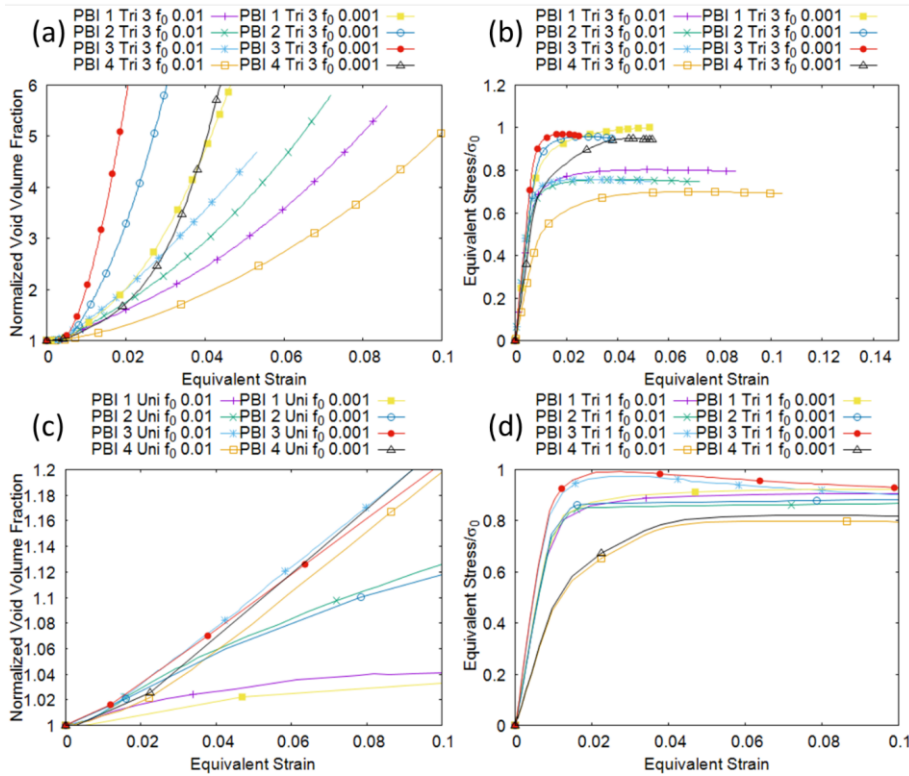
Figure 27: Effect of f_0 on evolution of VVF at $X=1/3$ (a) and $X=3$ (c) and on equivalent stress – equivlaent strain response at $X=1/3$ ($\sigma_0=1050$) (b) and $X=3$ ($\sigma_0=830$) (d)

4. Conclusions

Two different scenarios of the void growth were studied which can arise in multiphase titanium alloy (Ti-10V-2Fe-3Al). For the spherical void embedded in a single crystal of the α-phase of a multiphase titanium alloy Ti-10V-2Fe-3Al:

- Void growth rate increases exponentially with the increase in applied stress triaxiality.
- It was found that the void grows exponentially with applied equivalent strain for all values of stress triaxialities, except in the case of $X=1$ where it increases exponentially initially then the rate slows down because the matrix material starts to undergo considerable plastic deformation which dissipates the energy resulting in lower void growth.
- The void volume fraction increases faster for voids with low initial porosity as compared to higher initial porosity at all the stress triaxialities and crystal orientations.
- Void growth is affected by the crystal orientation at all the stress triaxialities. Stiffer configurations tend to have higher void growth due to higher stress concentration around void and higher pressure stress for same stress triaxiality.
- Void growth is significantly affected by the Lode parameter. As the value of the Lode parameter was increased from -1 to 1, the void growth rate was found to decrease for the tested crystal orientations.

27

- The void growth rate for the same Lode parameter value strongly depends on crystal orientation.
- Void growth affects the equivalent stress – equivalent strain response of the material.
- Higher stress triaxialities lead to higher softening because of higher void growth. Higher stress triaxiality decreases the yield strength as well as decreases the hardening rate of crystal.
- Softening due to void growth is higher in voids with higher initial porosity.
- Softening is higher in the case of single crystals containing void, with stiffer crystal orientations because of higher void growth.
- Increase in the Lode parameter leads to softer response. The amount of softening depends on the crystal orientation. The yield strength was reduced to half with a change of Lode parameter from -1 to 1 in case of ~~harder~~ stronger crystal orientation.

Void growth in dual-phase titanium alloys was simulated using an RVE having a spherical void at the interface of two phases. Properties of the α and β phases of Ti-10V-2Fe-3Al were assigned to each of these halves. It was found that:

- Similar to single α-phase crystal, the void volume fraction was found to increase exponentially with the increase in applied equivalent strain and the stress triaxiality.
- Phase boundary inclination (angle between major loading direction and normal to the phase boundary) plays an important role in the void growth in bicrystal. When the PBI was moved from 90° towards 0°, the void growth accelerated at all stress triaxialities and initial porosities.
- For PBI = 0°, the void growth rate becomes even lower than that of PBI = 90°, at higher stress triaxiality (3). But the void growth rate tends to increase with respect to other PBIs as the stress triaxiality is lowered. These behaviours are attributed to the variation in the slip activity around the void because of stress concentration due to crystal orientations and PBI.
- Slip activity because of void growth in the β phase was found to be higher at all PBIs except for PBI = 0° where it was lower than that of α.
- The equivalent stress –equivalent strain response in bicrystals (dual phase α-β) is found to be affected by PBI. Two phenomena, i.e. higher void growth in high strength crystal and difference in deformation in each of the two crystals due to PBI, are at play in case of bicrystals (α and β phases) which affects the material response as discussed in previous section.
- The BOR variant also influences the void growth at X=1 due to variation in slip activity in 3 sets of 4 BOR variants each and it affects the equivalent stress – equivalent strain response as well.
- The BOR variants in each of these 3 groups have equal void growth, these corresponds to β phase interface planes which have 90° angle between them about their intersection line.
- Initial porosity has a similar effect as was found in the case of single crystal of α phase, i.e. smaller initial porosity leads to higher void growth as compared to higher porosity at higher stress triaxialities
- In uniaxial case higher initial porosity have larger void growth because the void collapse in β phase is higher in lower initial porosity.

Acknowledgement

28

References

Alharbi, H.F., Kalidindi, S.R., 2015. Crystal plasticity finite element simulations using a database of discrete Fourier transforms. Int. J. Plast. 66, 71–84. https://doi.org/https://doi.org/10.1016/j.ijplas.2014.04.006

Aoyagi, Y., Tsuru, T., Shimokawa, T., 2014. Crystal plasticity modeling and simulation considering the behavior of the dislocation source of ultrafine-grained metal. Int. J. Plast. 55, 43–57. https://doi.org/https://doi.org/10.1016/j.ijplas.2013.09.009

Asim, U., Siddiq, M.A., Demiral, M., 2017. Void growth in high strength aluminium alloy single crystals: a CPFEM based study. Model. Simul. Mater. Sci. Eng. 25, 035010. https://doi.org/10.1088/1361-651X/aa5bcc

Barbe, F., Quey, R., 2011. A numerical modelling of 3D polycrystal-to-polycrystal diffusive phase transformations involving crystal plasticity. Int. J. Plast. 27, 823–840. https://doi.org/https://doi.org/10.1016/j.ijplas.2010.09.008

Barsoum, I., Faleskog, J., 2011. Micromechanical analysis on the influence of the Lode parameter on void growth and coalescence. Int. J. Solids Struct. 48, 925–938. https://doi.org/10.1016/J.IJSOLSTR.2010.11.028

Basirat, M., Shrestha, T., Potirniche, G.P., Charit, I., Rink, K., 2012. A study of the creep behavior of modified 9Cr–1Mo steel using continuum-damage modeling. Int. J. Plast. 37, 95–107. https://doi.org/10.1016/J.IJPLAS.2012.04.004

Benzerga, A.A., Besson, J., 2001. Plastic potentials for anisotropic porous solids. Eur. J. Mech. A/Solids 20, 397–434. https://doi.org/10.1016/S0997-7538(01)01147-0

Benzerga, A.A., Leblond, J.-B., 2010. Ductile Fracture by Void Growth to Coalescence.pdf. Adv. Appl. Mech. 44, 169-- 305.

Besson, J., 2009. Damage of ductile materials deforming under multiple plastic or viscoplastic mechanisms. Int. J. Plast. 25, 2204–2221. https://doi.org/https://doi.org/10.1016/j.ijplas.2009.03.001

Bhattacharjee, A., Varma, V.K., Kamat, S. V, Gogia, a K., Bhargava, S., 2006. Influence of b Grain Size on Tensile Behavior and Ductile Fracture Toughness of Titanium Alloy Ti-10V-2Fe-3Al. Metall. Mater. Trans. A 37, 1423. https://doi.org/10.1007/s11661-006-0087-x

Bhattacharyya, D., Viswanathan, G.., Denkenberger, R., Furrer, D., Fraser, H.L., 2003. The role of crystallographic and geometrical relationships between α and β phases in an α/β titanium alloy. Acta Mater. 51, 4679–4691. https://doi.org/10.1016/S1359-6454(03)00179-4

Borg, U., Niordson, C.F., Kysar, J.W., 2008. Size effects on void growth in single crystals with distributed voids. Int. J. Plast. 24, 688–701. https://doi.org/10.1016/j.ijplas.2007.07.015

Bridier, F., McDowell, D.L., Villechaise, P., Mendez, J., 2009. Crystal plasticity modeling of slip activity in Ti–6Al–4V under high cycle fatigue loading. Int. J. Plast. 25, 1066–1082. https://doi.org/https://doi.org/10.1016/j.ijplas.2008.08.004

Chen, W., Song, Z., Sun, Q., Xiao, L., She, W., Sun, J., Ge, P., 2010. Effect of Solution Treatment Temperature on Trigger Stress for Stress Induced Martensitic Transformation in Ti-10V-2Fe-3Al Alloy. J. Solid Mech. Mater. Eng. 4, 1296–1305. https://doi.org/10.1299/jmmp.4.1296

Choi, S.-H., Kim, D.W., Seong, B.S., Rollett, A.D., 2011. 3-D simulation of spatial stress distribution in an AZ31 Mg alloy sheet under in-plane compression. Int. J. Plast. 27, 1702–1720. https://doi.org/https://doi.org/10.1016/j.ijplas.2011.05.014

Danas, K., Ponte Castañeda, P., 2012. Influence of the Lode parameter and the stress triaxiality on the failure of elasto-plastic porous materials. Int. J. Solids Struct. 49, 1325–1342. https://doi.org/10.1016/J.IJSOLSTR.2012.02.006

Dunand, M., Mohr, D., 2014. Effect of Lode parameter on plastic flow localization after proportional loading at low stress triaxialities. J. Mech. Phys. Solids 66, 133–153. https://doi.org/10.1016/J.JMPS.2014.01.008

El Sayed, T., Gürses, E., Siddiq, M.A., 2012. A phenomenological two-phase constitutive model for porous shape memory alloys. Comput. Mater. Sci. 60, 44–52. https://doi.org/10.1016/J.COMMATSCI.2012.02.031

Erinosho, T.O., Dunne, F.P.E., 2015. Strain localization and failure in irradiated zircaloy with crystal plasticity. Int. J. Plast. 71, 170–194. https://doi.org/https://doi.org/10.1016/j.ijplas.2015.05.008

Fischer, F.D., Svoboda, J., 2014. Formation of bubbles by hydrogen attack and elastic–plastic deformation of the matrix. Int. J. Plast. 63, 110–123. https://doi.org/10.1016/J.IJPLAS.2013.10.007

Fleck, N.A., Hutchinson, J.W., 1993. A phenomenological theory for strain gradient effects in plasticity. J. Mech. Phys. Solids 41, 1825–1857. https://doi.org/10.1016/0022-5096(93)90072-N

Gao, X., Zhang, T., Zhou, J., Graham, S.M., Hayden, M., Roe, C., 2011. On stress-state dependent plasticity modeling: Significance of the hydrostatic stress, the third invariant of stress deviator and the non-associated flow rule. Int. J. Plast. 27, 217–231. https://doi.org/https://doi.org/10.1016/j.ijplas.2010.05.004

Ghosh, S., Anahid, M., 2013. Homogenized constitutive and fatigue nucleation models from crystal plasticity FE simulations of Ti alloys, Part 1: Macroscopic anisotropic yield function. Int. J. Plast. 47, 182–201. https://doi.org/https://doi.org/10.1016/j.ijplas.2012.12.008

Gologanu, M., Leblond, J.B., 1997. Recent extensions of Gurson's model for porous ductile metals, in: Suquet, P. (Ed.), Suquet, P. (Ed.), Continuum Micromechanics. Springer Vienna, Vienna, pp. 61–130. https://doi.org/10.1017/CBO9781107415324.004

Gologanu, M., Leblond, J.B., Devaux, J., 1993. Approximate models for ductile metals containing non-spherical voids-Case of axisymmetric prolate ellipsoidal cavities. J. Mech. Phys. Solids 41, 1723–1754. https://doi.org/10.1016/0022-5096(93)90029-F

Gonzalez, D., Simonovski, I., Withers, P.J., Quinta da Fonseca, J., 2014. Modelling the effect of elastic and plastic anisotropies on stresses at grain boundaries. Int. J. Plast. 61, 49–63. https://doi.org/https://doi.org/10.1016/j.ijplas.2014.03.012

Guo, H.J., Li, D.F., 2018. Crystal plasticity-based micromechanical finite element modelling of ductile void growth for an aluminium alloy under multiaxial loading conditions. Proc. Inst. Mech. Eng. Part L J. Mater. Des. Appl. 233, 56–62. https://doi.org/10.1177/1464420718805828

Gurson, A.L., 1977. Continuum Theory of Ductile Rupture by Void Nucleation and Growth: Part I-Yield criteria and Flow Rules for Porous Ductile Media. J. Eng. Mater. Technol. 99, 2–15. https://doi.org/10.1115/1.3443401

Ha, S., Kim, K., 2010. Void growth and coalescence in f.c.c. single crystals. Int. J. Mech. Sci. 52, 863–873. https://doi.org/10.1016/j.ijmecsci.2010.03.001

Hansen, B.L., Beyerlein, I.J., Bronkhorst, C.A., Cerreta, E.K., Dennis-Koller, D., 2013. A dislocation-based multi-rate single crystal plasticity model. Int. J. Plast. 44, 129–146.

https://doi.org/https://doi.org/10.1016/j.ijplas.2012.12.006

Herrera-Solaz, V., LLorca, J., Dogan, E., Karaman, I., Segurado, J., 2014. An inverse optimization strategy to determine single crystal mechanical behavior from polycrystal tests: Application to AZ31 Mg alloy. Int. J. Plast. 57, 1–15. https://doi.org/https://doi.org/10.1016/j.ijplas.2014.02.001

Hill, R., 1948. A Theory of the Yielding and Plastic Flow of Anisotropic Metals. Proc. R. Soc. London A Math. Phys. Eng. Sci. 193, 281–297. https://doi.org/10.1098/rspa.1948.0045

Huang, Y., 1991. Accurate Dilatation Rates for Spherical Voids in Triaxial Stress Fields. J. Appl. Mech. 58, 1084–1086. https://doi.org/10.1115/1.2897686

Hull, D., Rimmer, D.E., 1959. The growth of grain-boundary voids under stress. Philos. Mag. 4, 673–687. https://doi.org/10.1080/14786435908243264

Hutchinson, J.W., Tvergaard, V., 1989. Softening due to void nucleation in metals, in: Fracture Mechanics: Perspectives and Directions. ASTM International, p. 61.

Jeong, W., Lee, C.-H., Moon, J., Jang, D., Lee, M.-G., 2018. Grain Scale Representative Volume Element Simulation to Investigate the Effect of Crystal Orientation on Void Growth in Single and Multi-Crystals. Metals (Basel). 8. https://doi.org/10.3390/met8060436

Kadkhodapour, J., Butz, A., Ziaei-Rad, S., Schmauder, S., 2011. A micro mechanical study on failure initiation of dual phase steels under tension using single crystal plasticity model. Int. J. Plast. 27, 1103–1125. https://doi.org/https://doi.org/10.1016/j.ijplas.2010.12.001

Kalidindi, S.R., Anand, L., 1992. An approximate procedure for predicting the evolution of crystallographic texture in bulk deformation processing of fcc metals. Int. J. Mech. Sci. 34, 309–329. https://doi.org/https://doi.org/10.1016/0020-7403(92)90038-I

Kalidindi, S.R., Bronkhorst, C.A., Anand, L., 1992. Crystallographic texture evolution in bulk deformation processing of FCC metals. J. Mech. Phys. Solids 40, 537–569.

Kanamori, S., Abe, E., Tagawa, T., Chapetti, M.D., Miyata, T., 2007. EFFECTS OF MICROSTRUCTURE AND STRESS TRIAXIALITY ON DUCTILITY AND TOUGHNESS IN α/β TI ALLOYS. Growth (Lakeland) 1151, 802–807.

Kanamori, S., Abe, E., Tagawa, T., Miyata, T., 2013. Effects of constraint and grain size on ductility and toughness in Ti Alloys, in: ICF10, Honolulu (USA) 2001.

Kanamori, S., Abe, E., Tagawa, T., Miyata, T., 2002a. Size Effects of Fracture Toughness and Dependence of Microstructure in Ti-Alloys. J. Soc. Mater. Sci. Japan 51, 1352–1358. https://doi.org/10.2472/jsms.51.1352

Kanamori, S., Saito, M., Abe, E., Tagawa, T., Miyata, T., 2002b. Effects of Triaxiality and Microstructure on Ductile Fracture of α/β Titanium Alloys. J. Soc. Mater. Sci. Japan 51, 900–905. https://doi.org/10.2472/jsms.51.900

Khan, A.S., Liu, J., 2016. A deformation mechanism based crystal plasticity model of ultrafine-grained/nanocrystalline FCC polycrystals. Int. J. Plast. 86, 56–69. https://doi.org/https://doi.org/10.1016/j.ijplas.2016.08.001

Kim, J.H., Kim, D., Barlat, F., Lee, M.-G., 2012. Crystal plasticity approach for predicting the Bauschinger effect in dual-phase steels. Mater. Sci. Eng. A 539, 259–270. https://doi.org/10.1016/J.MSEA.2012.01.092

Kim, J.H., Lee, M.-G., Kang, J.-H., Oh, C.-S., Barlat, F., 2017. Crystal plasticity finite element analysis of

ferritic stainless steel for sheet formability prediction. Int. J. Plast. 93, 26–45. https://doi.org/https://doi.org/10.1016/j.ijplas.2017.04.007

Kiran, R., Khandelwal, K., 2014. A triaxiality and Lode parameter dependent ductile fracture criterion. Eng. Fract. Mech. 128, 121–138. https://doi.org/10.1016/J.ENGFRACMECH.2014.07.010

Kocks, U.F., Stout, M.G., Rollett, A.D., 1989. The Influence of Texture on Strain Hardening. Strength Met. Alloy. (ICSMA 8) 25–34. https://doi.org/10.1016/B978-0-08-034804-9.50008-5

Kohar, C.P., Bassani, J.L., Brahme, A., Muhammad, W., Mishra, R.K., Inal, K., 2017. A new multi-scale framework to incorporate microstructure evolution in phenomenological plasticity: Theory, explicit finite element formulation, implementation and validation. Int. J. Plast. https://doi.org/https://doi.org/10.1016/j.ijplas.2017.08.006

Leblond, J.-B., Perrin, G., Devaux, J., 1995. An improved Gurson-type model for hardenable ductile metals. Eur. J. Mech. A. Solids 14, 499–527.

Lecarme, L., Tekoğlu, C., Pardoen, T., 2011. Void growth and coalescence in ductile solids with stage III and stage IV strain hardening. Int. J. Plast. 27, 1203–1223. https://doi.org/https://doi.org/10.1016/j.ijplas.2011.01.004

Li, H., Fu, M.W., Lu, J., Yang, H., 2011. Ductile fracture: Experiments and computations. Int. J. Plast. 27, 147–180. https://doi.org/10.1016/J.IJPLAS.2010.04.001

Li, Z., Guo, W., 2002. The influence of plasticity mismatch on the growth and coalescence of spheroidal voids on the bimaterial interface. Int. J. Plast. 18, 249–279. https://doi.org/10.1016/S0749-6419(00)00078-4

Lim, H., Hale, L.M., Zimmerman, J.A., Battaile, C.C., Weinberger, C.R., 2015. A multi-scale model of dislocation plasticity in α-Fe: Incorporating temperature, strain rate and non-Schmid effects. Int. J. Plast. 73, 100–118. https://doi.org/https://doi.org/10.1016/j.ijplas.2014.12.005

Liu, B., Huang, Y., Li, M., Hwang, K.C., Liu, C., 2005. A study of the void size effect based on the Taylor dislocation model. Int. J. Plast. 21, 2107–2122. https://doi.org/10.1016/j.ijplas.2005.03.016

Liu, B., Qiu, X., Huang, Y., Hwang, K.C., Li, M., Liu, C., 2003. The size effect on void growth in ductile materials. J. Mech. Phys. Solids 51, 1171–1187. https://doi.org/10.1016/S0022-5096(03)00037-1

Liu, W.H., Zhang, X.M., Tang, J.G., Du, Y.X., 2007. Simulation of void growth and coalescence behavior with 3D crystal plasticity theory. Comput. Mater. Sci. 40, 130–139. https://doi.org/10.1016/j.commatsci.2006.11.009

Lütjering, G., Williams, J.C., 2007. Titanium : Engineering Materials and Processes, Edition SPRINGER. Springer. https://doi.org/10.1007/978-3-540-73036-1

Marin, E.B., 2006. On the Formulation of a Crystal Plasticity gModel. Sandia National Laboratories.

Mathur, K.K., Dawson, P.R., 1989. On modeling the development of crystallographic texture in bulk forming processes. Int. J. Plast. 5, 67–94. https://doi.org/10.1016/0749-6419(89)90020-X

Mayama, T., Noda, M., Chiba, R., Kuroda, M., 2011. Crystal plasticity analysis of texture development in magnesium alloy during extrusion. Int. J. Plast. 27, 1916–1935. https://doi.org/https://doi.org/10.1016/j.ijplas.2011.02.007

Mayeur, J.R., Beyerlein, I.J., Bronkhorst, C.A., Mourad, H.M., 2015. Incorporating interface affected zones into crystal plasticity. Int. J. Plast. 65, 206–225. https://doi.org/https://doi.org/10.1016/j.ijplas.2014.08.013

Monchiet, V., Bonnet, G., 2013. A Gurson-type model accounting for void size effects. Int. J. Solids Struct. 50, 320–327. https://doi.org/10.1016/j.ijsolstr.2012.09.005

Monchiet, V., Cazacu, O., Charkaluk, E., Kondo, D., 2008. Macroscopic yield criteria for plastic anisotropic materials containing spheroidal voids. Int. J. Plast. 24, 1158–1189. https://doi.org/10.1016/j.ijplas.2007.08.008

Monchiet, V., Charkaluk, E., Kondo, D., 2007. An improvement of Gurson-type models of porous materials by using Eshelby-like trial velocity fields. Comptes Rendus - Mec. 335, 32–41. https://doi.org/10.1016/j.crme.2006.12.002

Moody, N.R., Garrison, W.M., Costa, J.E., Smugeresky, J.E., 1989. The role of defect size on the fracture toughness of powder processed Ti-10V-2Fe-3Al. Scr. Metall. 23, 1147–1150. https://doi.org/10.1016/0036-9748(89)90316-5

Nielsen, K.L., Tvergaard, V., 2011. Failure by void coalescence in metallic materials containing primary and secondary voids subject to intense shearing. Int. J. Solids Struct. 48, 1255–1267. https://doi.org/10.1016/J.IJSOLSTR.2011.01.008

Niordson, C.F., Kysar, J.W., 2014. Computational strain gradient crystal plasticity. J. Mech. Phys. Solids 62, 31–47. https://doi.org/10.1016/j.jmps.2013.08.014

Niordson, C.F., Tvergaard, V., 2019. A homogenized model for size-effects in porous metals. J. Mech. Phys. Solids 123, 222–233. https://doi.org/https://doi.org/10.1016/j.jmps.2018.09.004

O'Regan, T.L., Quinn, D.F., Howe, M. a., McHugh, P.E., 1997. Void growth simulations in single crystals. Comput. Mech. 20, 115–121. https://doi.org/10.1007/s004660050226

Orsini, V.C., Zikry, M.A., 2001. Void growth and interaction in crystalline materials. Int. J. Plast. 17, 1393–1417. https://doi.org/10.1016/S0749-6419(00)00091-7

Peters, M., Kumpfert, J., Ward, C.H., Leyens, C., 2003. Titanium alloys for aerospace applications. Adv. Eng. Mater. 5, 419–427. https://doi.org/10.1002/adem.200310095

Popova, E., Staraselski, Y., Brahme, A., Mishra, R.K., Inal, K., 2015. Coupled crystal plasticity – Probabilistic cellular automata approach to model dynamic recrystallization in magnesium alloys. Int. J. Plast. 66, 85–102. https://doi.org/https://doi.org/10.1016/j.ijplas.2014.04.008

Potirniche, G.P., Hearndon, J.L., Horstemeyer, M.F., Ling, X.W., 2006. Lattice orientation effects on void growth and coalescence in fcc single crystals. Int. J. Plast. 22, 921–942. https://doi.org/10.1016/j.ijplas.2005.06.003

Prasad, N.S., Narasimhan, R., Suwas, S., 2017. Effects of lattice orientation and crack tip constraint on ductile fracture initiation in Mg single crystals. Int. J. Plast. 97, 222–245. https://doi.org/10.1016/J.IJPLAS.2017.06.004

Prasad, N.S., Narasimhan, R., Suwas, S., 2016. Numerical simulations of cylindrical void growth in Mg single crystals. Int. J. Fract. 200, 159–183. https://doi.org/10.1007/s10704-015-0063-9

Pushkareva, M., Adrien, J., Maire, E., Segurado, J., Llorca, J., Weck, A., 2016. Three-dimensional investigation of grain orientation effects on void growth in commercially pure titanium. Mater. Sci. Eng. A 671, 221–232. https://doi.org/10.1016/J.MSEA.2016.06.053

Quinn, D.F., Connolly, P.J., Howe, M.A., McHugh, P.E., 1997. Simulation of void growth in WC-Co hardmetals using crystal plasticity theory. Int. J. Mech. Sci. 39, 173–183. https://doi.org/10.1016/0020-7403(96)00051-3

Raghunathan, S.L., Stapleton, A.M., Dashwood, R.J., Jackson, M., Dye, D., 2007. Micromechanics of

Ti-10V-2Fe-3Al: In situ synchrotron characterisation and modelling. Acta Mater. 55, 6861–6872. https://doi.org/10.1016/j.actamat.2007.08.049

Rice, J.R., Tracey, D.M., 1969. On the ductile enlargement of voids in triaxial stress fields. J. Mech. Phys. Solids 17, 201–217. https://doi.org/10.1016/0022-5096(69)90033-7

Roy, S., Suwas, S., Tamirisakandala, S., Srinivasan, R., Miracle, D.B., 2012. Microstructure and texture evolution during β extrusion of boron modified Ti–6Al–4V alloy. Mater. Sci. Eng. A 540, 152–163. https://doi.org/10.1016/j.msea.2012.01.120

Savage, D.J., Chandola, N., Cazacu, O., McWilliams, B.A., Knezevic, M., 2018. Validation of recent analytical dilatational models for porous polycrystals using crystal plasticity finite element models with Schmid and non-Schmid activation laws. Mech. Mater. 126, 148–162. https://doi.org/10.1016/J.MECHMAT.2018.08.004

Segurado, J., LLorca, J., 2010. Discrete dislocation dynamics analysis of the effect of lattice orientation on void growth in single crystals. Int. J. Plast. 26, 806–819. https://doi.org/https://doi.org/10.1016/j.ijplas.2009.10.009

Shihong, W., Guiqin, S., 1990. Ti-10V-2Fe-3Al Alloy Solid Solution Ageing, Structure and Properties. Rare Met. Mater. Eng. 26–34.

Shu, J.Y., 1998. Scale-dependent deformation of porous single crystals. Int. J. Plast. 14, 1085–1107. https://doi.org/10.1016/S0749-6419(98)00048-5

Siddiq, M.A., 2018. A porous crystal plasticity constitutive model for ductile deformation and failure in porous single crystals. Int. J. Damage Mech. 28, 233–248. https://doi.org/10.1177/1056789518757294

Siddiq, M.A., Arciniega, R., El Sayed, T., 2012. A variational void coalescence model for ductile metals. Comput. Mech. 49, 185–195. https://doi.org/10.1007/s00466-011-0639-9

Siddiq, M.A., El Sayed, T., 2015. A multiscale phenomenological constitutive model for strain rate dependent tensile ductility in nanocrystalline metals. Mater. Lett. 142, 60–63. https://doi.org/10.1016/J.MATLET.2014.11.112

Siddiq, M.A., El Sayed, T., 2011. Acoustic softening in metals during ultrasonic assisted deformation via CP-FEM. Mater. Lett. 65, 356–359. https://doi.org/10.1016/j.matlet.2010.10.031

Siddiq, M.A., Ghassemieh, E., 2008. Thermomechanical analyses of ultrasonic welding process using thermal and acoustic softening effects. Mech. Mater. 40, 982–1000. https://doi.org/10.1016/J.MECHMAT.2008.06.004

Siddiq, M.A., Schmauder, S., 2006. Interface fracture analyses of a bicrystal niobium / alumina specimen using a cohesive modelling. Model. Simul. Mater. Sci. Eng. 14, 1015–1030. https://doi.org/10.1088/0965-0393/14/6/009

Siddiq, M.A., Schmauder, S., Huang, Y., 2007. Fracture of bicrystal metal/ceramic interfaces: A study via the mechanism-based strain gradient crystal plasticity theory. Int. J. Plast. 23, 665–689. https://doi.org/10.1016/j.ijplas.2006.08.007

Siddiq, M.A., Schmauder, S., Ruehle, M., 2008. Niobium/alumina bicrystal interface fracture: A theoretical interlink between local adhesion capacity and macroscopic fracture energies. Eng. Fract. Mech. 75, 2320–2332. https://doi.org/10.1016/j.engfracmech.2007.09.005

Simulia, D.S., 2012. Abaqus 6.12 documentation. Provid. Rhode Island, US.

Song, D., Ponte Castañeda, P., 2018. A multi-scale homogenization model for fine-grained porous

34

viscoplastic polycrystals: I – Finite-strain theory. J. Mech. Phys. Solids 115, 102–122. https://doi.org/10.1016/J.JMPS.2018.03.001

Song, D., Ponte Castañeda, P., 2017a. A finite-strain homogenization model for viscoplastic porous single crystals: I – Theory. J. Mech. Phys. Solids 107, 560–579. https://doi.org/10.1016/J.JMPS.2017.06.008

Song, D., Ponte Castañeda, P., 2017b. A finite-strain homogenization model for viscoplastic porous single crystals: I – Theory. J. Mech. Phys. Solids 107, 560–579. https://doi.org/10.1016/J.JMPS.2017.06.008

Stewart, J.B., Cazacu, O., 2011. Analytical yield criterion for an anisotropic material containing spherical voids and exhibiting tension-compression asymmetry. Int. J. Solids Struct. 48, 357–373. https://doi.org/10.1016/j.ijsolstr.2010.10.009

Su, Y., Zambaldi, C., Mercier, D., Eisenlohr, P., Bieler, T.R., Crimp, M.A., 2016. Quantifying deformation processes near grain boundaries in α titanium using nanoindentation and crystal plasticity modeling. Int. J. Plast. 86, 170–186. https://doi.org/10.1016/j.ijplas.2016.08.007

Suri, S., Viswanathan, G.B., Neeraj, T., Hou, D.-H., Mills, M.J., 1999. Room temperature deformation and mechanisms of slip transmission in oriented single-colony crystals of an α/β titanium alloy. Acta Mater. 47, 1019–1034. https://doi.org/10.1016/S1359-6454(98)00364-4

Tang, T., Kim, S., Horstemeyer, M.F., 2010. Molecular dynamics simulations of void growth and coalescence in single crystal magnesium. Acta Mater. 58, 4742–4759. https://doi.org/10.1016/J.ACTAMAT.2010.05.011

Tekoğlu, C., 2014. Representative volume element calculations under constant stress triaxiality, Lode parameter, and shear ratio. Int. J. Solids Struct. 51, 4544–4553. https://doi.org/10.1016/j.ijsolstr.2014.09.001

Tekoğlu, C., Hutchinson, J.W., Pardoen, T., 2015. On localization and void coalescence as a precursor to ductile fracture. Philos. Trans. R. Soc. A Math. Phys. Eng. Sci. 373, 20140121. https://doi.org/10.1098/rsta.2014.0121

Terlinde, G., Rathjen, H.-J., Schwalbe, K.-H., 1988. Microstructure and fracture toughness of the aged ‚β-Ti Alloy Ti-10V-2Fe-M. Metall. Trans. A 19, 1037–1049. https://doi.org/10.1007/BF02628388

Terlinde, G.T., Duerig, T.W., Williams, J.C., 1983. Microstructure, tensile deformation, and fracture in aged ti 10V-2Fe-3Al. Metall. Trans. A 14, 2101–2115. https://doi.org/10.1007/BF02662377

Terlinde, G.T., Duerig, T.W., Williams, J.C., 1980. The Effect of Heat Treatment on Microstructure and Tensile Properties of Ti-10V-2Fe-3Al. DTIC Document.

Thakare, A.G., Narasimhan, R., Mishra, R.K., 2009. Numerical simulations of void growth near a notch tip in ductile single crystals. Mech. Mater. 41, 506–519. https://doi.org/10.1016/J.MECHMAT.2009.01.007

Torki, M.E., Benzerga, A.A., 2018. A mechanism of failure in shear bands. Extrem. Mech. Lett. 23, 67–71. https://doi.org/10.1016/J.EML.2018.06.008

Tvergaard, V., 1989. Material Failure by Void Growth to Coalescence. Adv. Appl. Mech. 27, 83–151. https://doi.org/10.1016/S0065-2156(08)70195-9

Tvergaard, V., Needleman, A., 1984. Analysis of the cup-cone fracture in a round tensile bar. Acta Metall. 32, 157–169. https://doi.org/10.1016/0001-6160(84)90213-X

Upadhyay, M. V, Patra, A., Wen, W., Panzner, T., Van Petegem, S., Tomé, C.N., Lebensohn, R.A., Van

Swygenhoven, H., 2018. Mechanical response of stainless steel subjected to biaxial load path changes: Cruciform experiments and multi-scale modeling. Int. J. Plast. 108, 144–168. https://doi.org/https://doi.org/10.1016/j.ijplas.2018.05.003

Williams, J.C., Baggerly, R.G., Paton, N.E., 2002. Deformation behavior of HCPTi-Al alloy single crystals. Metall. Mater. Trans. a-Physical Metall. Mater. Sci. 33, 837–850. https://doi.org/10.1007/s11661-002-1016-2

Xie, R., Lin, N., Zhou, P., Zou, J., Han, P., Wang, Z., Tang, B., 2018. Surface damage mitigation of TC4 alloy via micro arc oxidation for oil and gas exploitation application: Characterizations of microstructure and evaluations on surface performance. Appl. Surf. Sci. 436, 467–476. https://doi.org/10.1016/J.APSUSC.2017.12.047

Yang, M., Dong, X., 2009. Simulation of lattice orientation effects on void growth and coalescence by crystal plasticity. Acta Metall. Sin. (English Lett. 22, 40–50. https://doi.org/10.1016/S1006-7191(08)60069-1

Yerra, S.K., Tekoğlu, C., Scheyvaerts, F., Delannay, L., Van Houtte, P., Pardoen, T., 2010. Void growth and coalescence in single crystals. Int. J. Solids Struct. 47, 1016–1029. https://doi.org/10.1016/J.IJSOLSTR.2009.12.019

Yu, Q.M., Hou, N.X., Yue, Z.F., 2010. Finite element analysis of void growth behavior in nickel-based single crystal superalloys. Comput. Mater. Sci. 48, 597–608. https://doi.org/10.1016/J.COMMATSCI.2010.02.028

Zeng, W.D., Zhou, Y.G., 1999. Effect of beta flecks on mechanical properties of Ti–10V–2Fe–3Al alloy. Mater. Sci. Eng. A 260, 203–211. https://doi.org/10.1016/S0921-5093(98)00954-X

Zhang, K., Holmedal, B., Hopperstad, O.S., Dumoulin, S., Gawad, J., Van Bael, A., Van Houtte, P., 2015. Multi-level modelling of mechanical anisotropy of commercial pure aluminium plate: Crystal plasticity models, advanced yield functions and parameter identification. Int. J. Plast. 66, 3–30. https://doi.org/https://doi.org/10.1016/j.ijplas.2014.02.003

Zhang, K.S., Bai, J.B., François, D., 2001. Numerical analysis of the influence of the Lode parameter on void growth. Int. J. Solids Struct. 38, 5847–5856. https://doi.org/10.1016/S0020-7683(00)00391-7

Zhang, Z., Lunt, D., Abdolvand, H., Wilkinson, A.J., Preuss, M., Dunne, F.P.E., 2018. Quantitative investigation of micro slip and localization in polycrystalline materials under uniaxial tension. Int. J. Plast. 108, 88–106. https://doi.org/https://doi.org/10.1016/j.ijplas.2018.04.014

Zhou, J., Gao, X., Sobotka, J.C., Webler, B.A., Cockeram, B. V., 2014. On the extension of the Gurson-type porous plasticity models for prediction of ductile fracture under shear-dominated conditions. Int. J. Solids Struct. 51, 3273–3291. https://doi.org/10.1016/j.ijsolstr.2014.05.028